



A deep learning approach for detection of shallow anterior chamber depth based on the hidden features of fundus photographs



Tae Keun Yoo^{a,b,*}, Ik Hee Ryu^{a,c}, Jin Kuk Kim^{a,c}, In Sik Lee^a, Hong Kyu Kim^d

^a B&VIIT Eye Center, Seoul, South Korea

^b Department of Ophthalmology, Aerospace Medical Center, Republic of Korea Air Force, Cheongju, South Korea

^c VISUWORKS, Seoul, South Korea

^d Department of Ophthalmology, Dankook University Hospital, Dankook University College of Medicine, Cheonan, South Korea

ARTICLE INFO

Article history:

Received 14 August 2021

Revised 15 February 2022

Accepted 4 March 2022

Keywords:

Shallow anterior chamber depth

Fundus photographs

Deep learning

CycleGAN

Characteristic feature map

ABSTRACT

Background and Objectives: Patients with angle-closure glaucoma (ACG) are asymptomatic until they experience a painful attack. Shallow anterior chamber depth (ACD) is considered a significant risk factor for ACG. We propose a deep learning approach to detect shallow ACD using fundus photographs and to identify the hidden features of shallow ACD.

Methods: This retrospective study assigned healthy subjects to the training ($n = 1188$ eyes) and test ($n = 594$) datasets (prospective validation design). We used a deep learning approach to estimate ACD and build a classification model to identify eyes with a shallow ACD. The proposed method, including subtraction of the input and output images of CycleGAN and a thresholding algorithm, was adopted to visualize the characteristic features of fundus photographs with a shallow ACD.

Results: The deep learning model integrating fundus photographs and clinical variables achieved areas under the receiver operating characteristic curve of 0.978 (95% confidence interval [CI], 0.963–0.988) for an $ACD \leq 2.60$ mm and 0.895 (95% CI, 0.868–0.919) for an $ACD \leq 2.80$ mm, and outperformed the regression model using only clinical variables. However, the difference between shallow and deep ACD classes on fundus photographs was difficult to be detected with the naked eye. We were unable to identify the features of shallow ACD using the Grad-CAM. The CycleGAN-based feature images showed that area around the macula and optic disk significantly contributed to the classification of fundus photographs with a shallow ACD.

Conclusions: We demonstrated the feasibility of a novel deep learning model to detect a shallow ACD as a screening tool for ACG using fundus photographs. The CycleGAN-based feature map showed the hidden characteristic features of shallow ACD that were previously undetectable by conventional techniques and ophthalmologists. This framework will facilitate the early detection of shallow ACD to prevent overlooking the risks associated with ACG.

© 2022 Elsevier B.V. All rights reserved.

1. Introduction

Anterior chamber depth (ACD) refers to the distance between the corneal endothelium and the anterior capsule surface of the crystalline lens. A shallow ACD is considered a significant risk factor for primary angle-closure glaucoma (ACG) [1]. In an eye with ACG, increased intraocular pressure (IOP) occurs when the iris blocks the drainage of the aqueous humor. Eyes with a shallow ACD have a more crowded anterior segment with narrow drainage

angles and are more likely to develop ACG than those with deep ACD. An elevated IOP may lead to severe pain, irreversible optic nerve damage, and blindness [2]. According to the literature, blindness is estimated to be present in approximately 4 million patients with ACG worldwide [3]. Many people with ACG are asymptomatic until they experience a sudden increase in IOP. ACG is generally treated with laser peripheral iridotomy to prevent sudden or chronic blockage of aqueous humor drainage [4]. In addition, it has been established that shallow ACD is critically associated with intraoperative complications of cataract surgery and poor clinical outcomes [5]. Thus, patients should be informed of their ACD status after the eye examination.

The early detection of patients with shallow ACD is essential for the management of ACG and cataract surgery [6]. Methods to

* Corresponding author at: Department of Ophthalmology, Aerospace Medical Center, Korea Air Force, Cheongju, 635 Danjae-ro, Namil-myeon, Cheongwon-gun, Chungcheongbuk-do 363-849, South Korea.

E-mail addresses: fawoo2@yonsei.ac.kr, eyetaekeunyoo@gmail.com (T.K. Yoo).

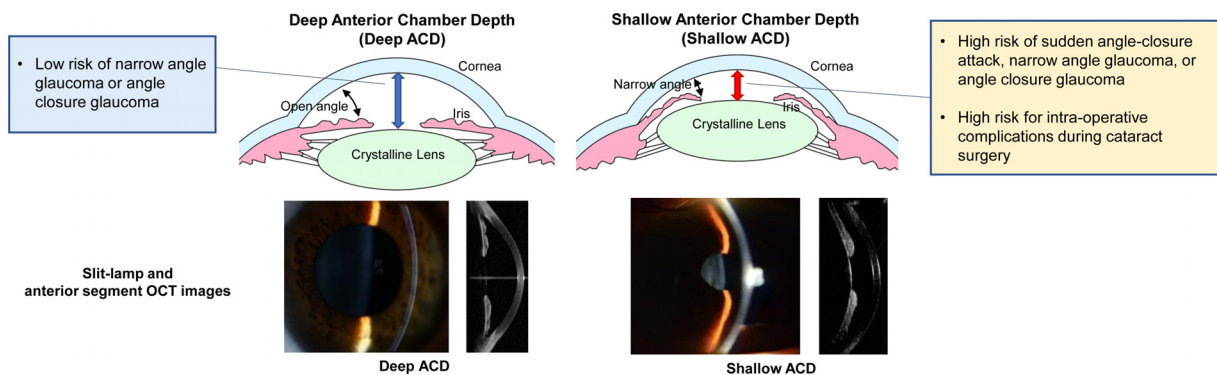


Fig. 1. Definition of a deep versus shallow anterior chamber depth and related medical conditions. Our study aimed to correlate findings on fundus photographs (posterior pole of the eye) to depth of the anterior chamber (anterior segment of the eye). ACD, anterior chamber depth; OCT, optical coherence tomography.

measure ACD using ultrasound biometry, pentacam imaging, and anterior segment optical coherence tomography (OCT) have become available in clinics [7]. However, ultrasonography is not reproducible, and other methods require bulky equipment that is inappropriate for population screening [8]. Most devices used for anterior segment imaging are expensive. Anterior segment imaging techniques are not used in most medical check-ups because current ACD measurements are time-consuming and dependent on the operator's skill. Novel methods based on artificial intelligence (AI) were recently adopted to screen for a shallow ACD or ACG using anterior segment imaging. Most deep learning studies have focused on automated angle-closure detection in cross-sectional images from anterior segment OCT [9] and ultrasonography images [10]. Although these techniques improve diagnostic performance, they are not ideal for population-based screenings of shallow ACD or ACG because of the aforementioned problems of measuring equipment.

Color fundus photography is an effective tool for screening for ocular diseases and has been widely used in eye clinics and health check-up centers. There has been a surge in deep learning research for detecting several healthcare conditions using fundus photographs [11]. Deep learning can detect many ophthalmic diseases, including rare pathological conditions [12], and it shows comparable performance to that of human experts [13]. Recently, deep learning has been used to analyze retinal photographs for predicting cardiovascular diseases, which were previously considered unrelated to retinal image findings [14]. Refractive error can also be estimated using fundus photographs using a deep learning technique [15]. Furthermore, deep learning can combine fundus photographs and systemic health variables to predict IOP [16]. These studies have shown that fundus photographs provide information about a patient's retinal structure as well as various systemic health conditions. This concept could be extended to the measurement of ACD and evaluation of the risk of ACG.

Here, we propose a deep learning approach to detect a shallow ACD using fundus photographs. As shown in Fig. 1, even if the anterior chamber is very small, a slight difference in ACD could indicate a significant anatomical and pathological change of the eye. The ability to detect a shallow ACD using only fundus photographs will benefit in medical check-ups and eye clinics that do not have expensive equipment for ACD measurements. In addition, we proposed a medical application of a cycle-consistency generative adversarial network (CycleGAN) and a thresholding technique to generate a characteristic feature map. The innovation and contributions of this study are:

- 1) We propose a novel application of deep learning with fundus photographs for detecting a shallow ACD. Our framework can

link the posterior segment information (from the retina) to the anterior segment of the eye (ACD).

- 2) The CycleGAN-based feature map generation provides new insights into retinal image patterns of ACD, which is very subtle and difficult to detect with the naked eye. Image subtraction and Otsu thresholding techniques successfully visualized the feature changes of fundus photographs for shallow ACD.

2. Methods

2.1. Datasets

We retrospectively collected clinical data and fundus photographs from the B&VIIT Eye Center, Seoul, South Korea. The retrospective study protocol was approved by the Institutional Review Board of the Korean National Institute for Bioethics Policy. Informed consent was waived by the review board due to the study design. This study adhered to the tenets of the Declaration of Helsinki. The current study analyzed the preoperative ocular data of healthy subjects who intended to undergo refractive surgery at the B&VIIT Eye Center between January 2015 and December 2016. All patients underwent preoperative measurements of best-corrected visual acuity, manifest refraction, and slit-lamp examination of the anterior segment [17]. We used macula-centered fundus photographs of the posterior pole of the eyes that were obtained during the preoperative examination. Non-mydriatic fundus photographs were taken using two different retinal cameras, including a Maestro 2 non-mydriatic retinal camera (Topcon Corporation, Tokyo, Japan) and a CR-2 non-mydriatic retinal camera (Canon, Tokyo, Japan). A non-contact tonometry and pachymetry device (NT-530P; Nidek Co., Ltd., Aichi, Japan) was used to evaluate IOP and central corneal thickness. Trained medical workers and ophthalmologists performed all measurements.

The inclusion criteria for this study were as follows: age between 20 and 50 years, stable refraction, +5.00 to -20.00 diopters of hyperopia or myopia with astigmatism of 5.00 D or less, and availability of fundus photographs. Subjects with a history of previous ocular surgery, corneal diseases, glaucoma, uveitis, and retinal diseases were excluded from the study. This study ultimately included 1782 eyes of 891 healthy subjects with no history of refractive surgery. The dataset contains their preoperative measurements. As shown in Fig. 2, for the prospective validation design via chronological splitting [18], we assigned the subjects who visited before April 2016 (66.7%, n = 1188 eyes of 594 subjects) to the training dataset and those who visited after May 2016 (33.3%, n = 594 eyes of 297 subjects) to the test validation dataset. Chronological splitting helps evaluate the generalizability of the prediction models with respect to the potential changes in clinical practice and patients across time (generalizability of future unseen

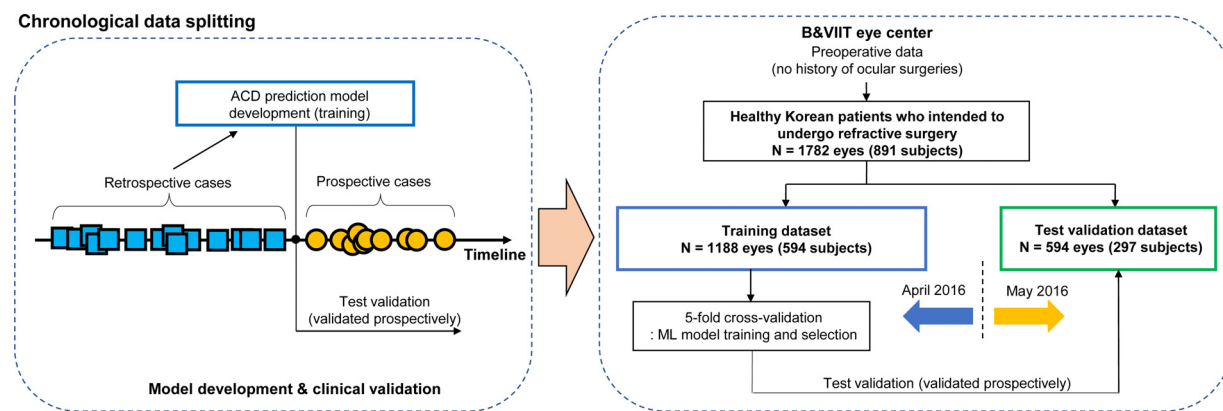


Fig. 2. Data management for training models and validation. Chronological splitting into retrospective and prospective cases helped evaluate the generalizability of the prediction models with respect to potential changes in clinical practice and patients across time.

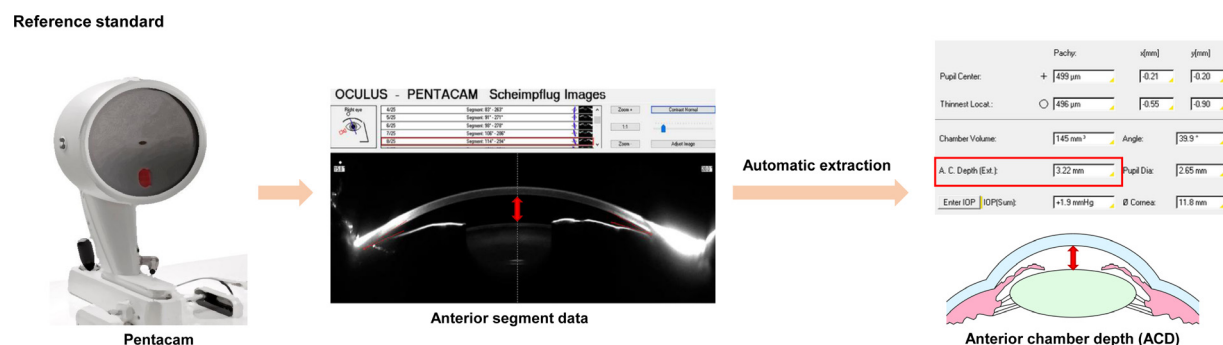


Fig. 3. Anterior chamber depth (ACD) measurement using a pentacam HR Scheimpflug device. In this study, the ACD measurement is considered as a reference standard.

data) [19]. We performed five-fold cross-validation in the training process, the preferred technique for assessing performance and optimizing prediction models, similar to the previous study [17].

2.2. Definition of a shallow ACD (reference standard)

In this study, the ACD measurement is considered as a reference standard. As shown in Fig. 3, ACD was measured using a pentacam HR Scheimpflug device (Oculus Optikgeräte GmbH, Wetzlar, Germany). Currently, there is a lack of a universal definition of shallow ACD due to ethnic differences. In this study, we defined a shallow ACD as an ACD measurement of 2.80 mm or lower according to a previous study [20]. This criterion was adopted for the classification and feature map generation. Additionally, we built a classification model for predicting a shallower ACD (2.60 mm or lower) to detect more severe cases. To simplify the categorization, non-shallow ACD eyes were referred to as “deep ACD” in this study. Because all of these processes were performed by objective measurements from the pentacam device, no pixel or image-level manual annotations for segmentation were used in this study.

2.3. Deep learning algorithm

The study objective and algorithm development processes are illustrated in Fig. 4. We adopted three machine learning approaches to build the classification models to identify eyes with shallow ACD. First, we analyzed the clinical variables, including age, sex, refractive error, IOP, and central corneal thickness, using a machine learning approach without fundus photographs. Second, we used convolutional neural network (CNN) architectures to analyze fundus photographs without clinical variables. Third, we

adopted a two-stage machine learning technique to integrate the clinical variables and fundus photography. In the later stage of the combined model, a machine learning technique combined clinical variables and the outputs of a CNN model, which was trained using fundus photography in the earlier stage. Logistic regression, a one-hidden-layer feedforward artificial neural network (FFANN) with ten hidden nodes and sigmoid activation, and an XGBoost algorithm were used to integrate all factors, including preoperative clinical variables and the soft-max output of ResNet50 based on fundus photography. XGBoost falls under a larger parallel decision tree, boosting and optimizing the model's training loss and regularization for the ensemble of trees generated [21]. We evaluated multiple hyperparameter conditions in earlier experiments and empirically found that the optimal model of XGBoost corroborated that the learning rate corresponded to 0.1, maximum tree depth for base learners corresponded to 5, and γ corresponded to 0.001.

The CNN model consists of two parts: a CNN feature encoder module and a fully connected layer module, similar to a previous studies [22,23]. A pretrained network based on conventional CNN architectures was adopted as the feature extractor. This neural network architecture was pre-trained on the ImageNet database and imported into MATLAB R2020b (MathWorks Inc., Natick, MA, USA) platform. Pretrained CNN architectures were extensively and successfully used in previous studies involving ophthalmic disease detection using fundus photography and have shown state-of-the-art performance [24]. The input images were resized to the original input tensor of each CNN architecture. In our task, the last layers of the CNN architectures were replaced with a modified fully connected layer (with 2×2048 wt and 2×1 bias for ResNet50) and a softmax function layer for two classes, which set the output

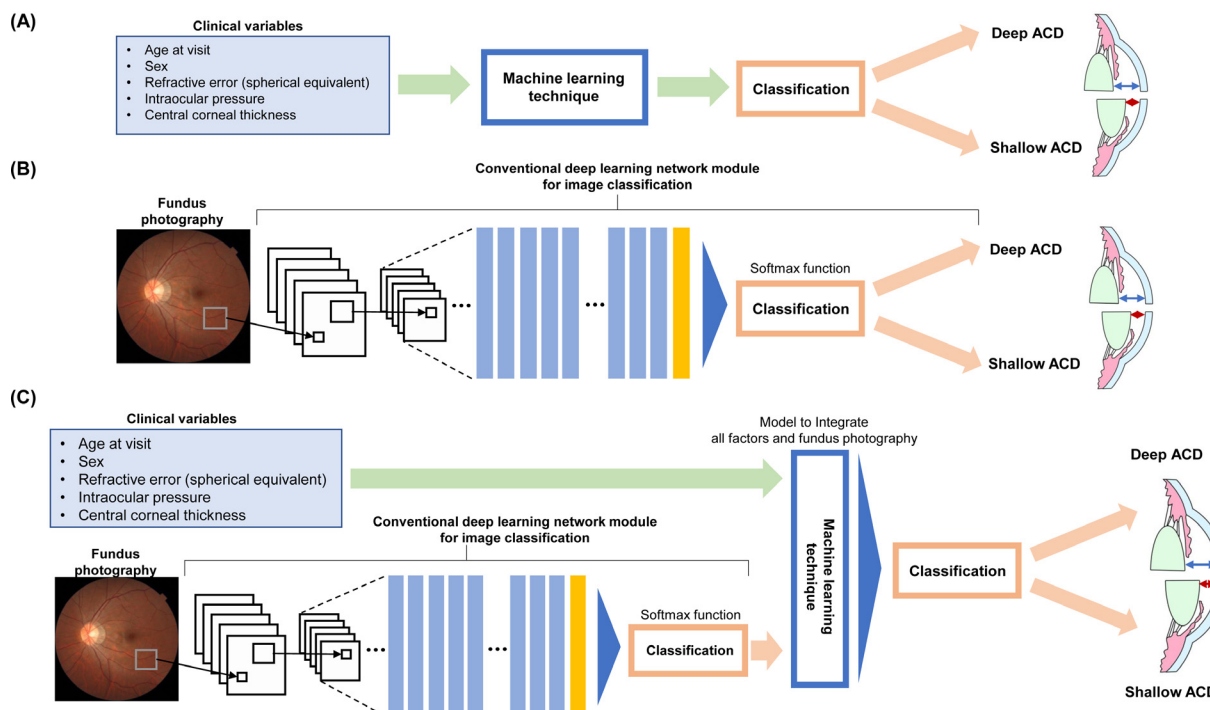


Fig. 4. Schematic of the deep learning algorithm using fundus photographs to predict shallow ACD. (A) A machine learning model using clinical variables including age, sex, refractive error, intraocular pressure, and central corneal thickness. (B) A convolutional neural network (deep learning) model using fundus photography. (C) A combined machine learning model integrating clinical variables and fundus photography. ACD, anterior chamber depth.

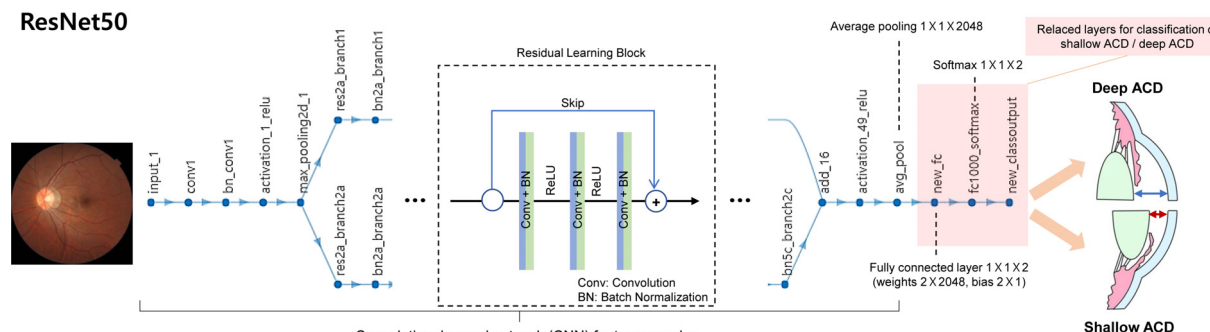


Fig. 5. The detailed architecture of ResNet50 used to predict shallow ACD from fundus photography. ACD, anterior chamber depth.

of the classification result to a range of 0–1, and corresponds to the predicted probability of shallow and deep ACD classes. The detailed CNN architecture of ResNet50 as an example for this study is shown in Fig. 5. The cross-entropy loss function for the CNN classification task is defined as:

$$L_{\text{Cross Entropy}} = - \sum_i^N p_i \log(q_i)$$

where p_i represents the ground truth value (shallow or deep ACD), and q_i represents the predicted probability value from a classifier for the i th image. During the training, to prevent overfitting, data augmentation was performed using linear transformation including left and right flip, width and height translation from -5% to $+5\%$, random rotation from -30° to 30° , zooming from 0 to 10%, and a random brightness change from -10% to 10% . The model was optimized with Adam with a batch size of 20, a base default learning parameters for transfer learning (learning rate = 0.00001, $\beta_1 = 0.9$, and $\beta_2 = 0.999$) during an epoch of 100. The optimizer updates the network parameters to minimize loss function. In our

experiments, we tuned the entire network parameters of the CNN using the training dataset. We chose the final classifier model that maximized the accuracy of the validation dataset. A saliency map was generated using the Grad-CAM technique from the ResNet50 model, the most widely used AI technique [25], to visualize the characteristic features of shallow and deep ACD for interpretability. In this study, we focused on ResNet50, but DarkNet-53 and EfficientNet-B0 were also trained and evaluated for the same task for the comparative analysis.

2.4. Feature map generation

The conventional saliency map from Grad-CAM shows the approximate location on which the model focuses on, but it is unable to indicate the detailed features of the class [26]. To overcome this disadvantage, we propose a novel medical application of the CycleGAN technique to obtain a feature map of shallow ACD in a fundus photograph. It should be noted that the CycleGAN-based model and the CNN model described earlier are different and indepen-

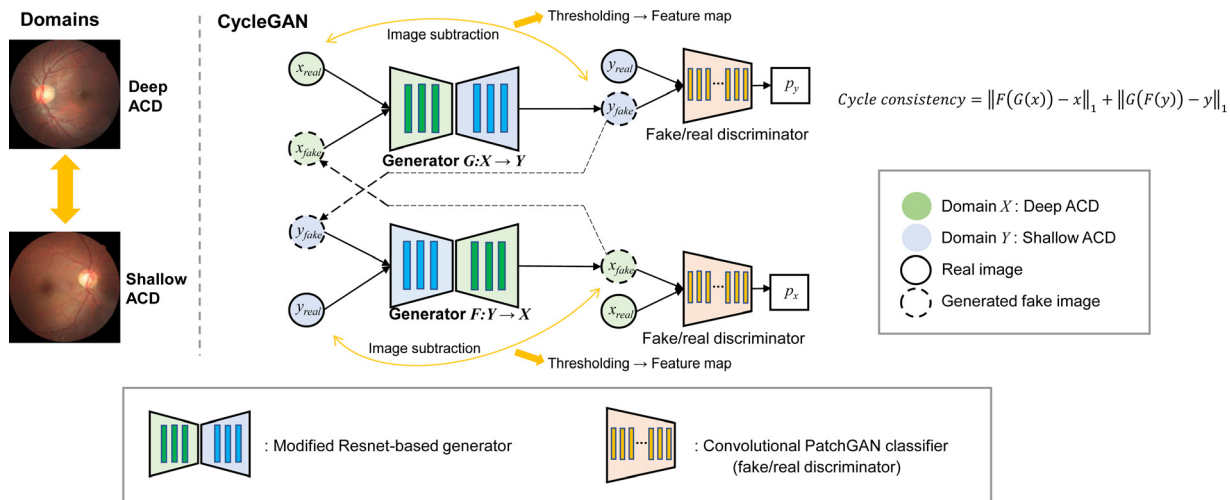


Fig. 6. Schematic of the CycleGAN-based feature map generation for fundus photographs with shallow and deep anterior chamber depth (ACD). The detailed structure of the convolutional PatchGAN classifier is shown in the Supplementary Materials.

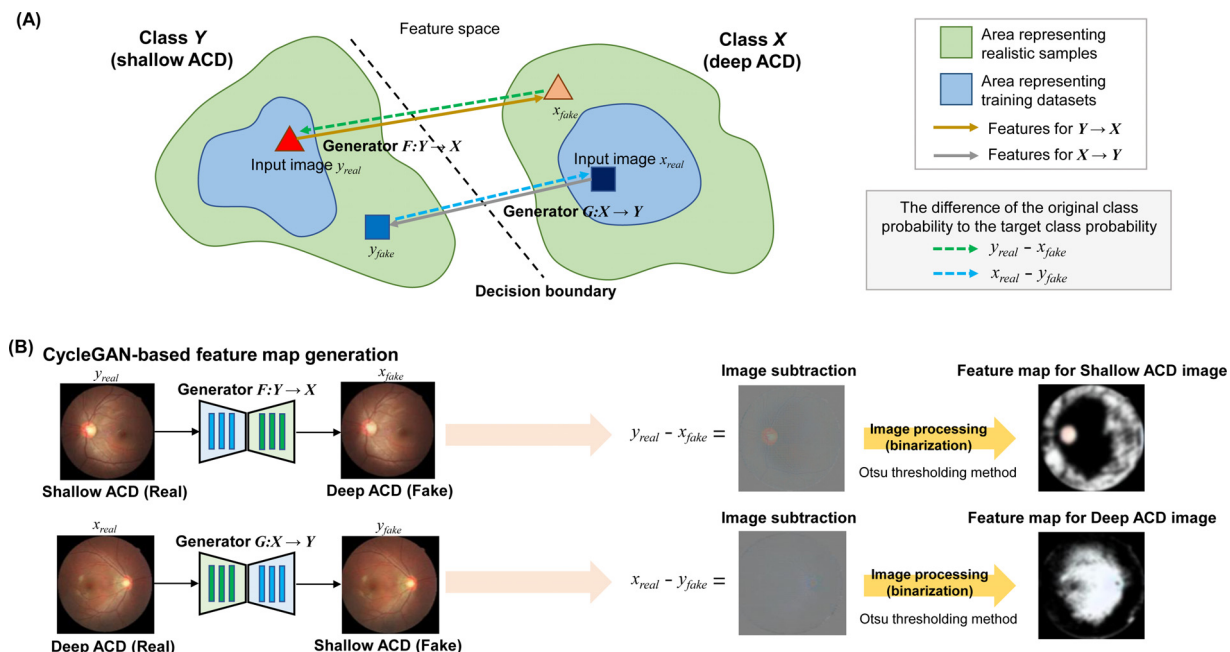


Fig. 7. A conceptual illustration of CycleGAN-based explanation about decision boundary and image features of our dataset. (A) The CycleGAN helps transfer the sample into the realistic sample space. The difference between the original and target classes could be considered as the attributes of original class. This technique is similar to the GAN-based explanation that was proposed to improve saliency map [28]. (B) Feature image generation using generators from CycleGAN and Otsu thresholding algorithm.

dent architectures, and CycleGAN is introduced to explain the pixel distribution in the dataset. The architecture of the proposed CycleGAN model is shown in Fig. 6 [27]. Using CycleGAN, a fundus photograph of a shallow ACD class can be automatically transferred to a realistic image of a deep ACD class. The difference between the original and generated images contains the gradient information between two domains. We have extended this concept and hypothesized that the difference between the original shallow ACD image and the transferred image of a deep ACD can be used as a feature map of a shallow ACD. The conceptual illustration and feature map generation processes are shown in Fig. 7. A previous study proposed a GAN-based attribution method to identify the key features of the samples [28]. Our method is similar to this GAN-based attribution technique as it also provides key features by calculating the difference between the dataset's original class probability and

its target class probability. The GAN can obtain the closest realistic example to calculate the realistic difference between the two domains. We subtracted the input and output images of CycleGAN and adopted a thresholding algorithm to identify the characteristic features (see Supplementary Materials).

The core concept of CycleGAN is that an image that is translated from one class to another by one generator model and translated back again by a different generator model should be identical to the original image [27]. The learning process of CycleGAN mathematically maps the features of the data distribution between source class X and target class Y . For instance, in the present study, the source class X could denote a deep ACD and the target class Y could denote a shallow ACD. This technique includes two image generators, namely, $G_{X \rightarrow Y}$ and $F_{Y \rightarrow X}$, and two image discriminators, namely, D_X and D_Y . These discriminators were trained to

distinguish between the synthetic samples generated by the mapping functions and the real samples in each class. In CycleGAN, the mapping functions G and F have cycle consistency, which means that the image translation cycle can bring an image x from class X back to the original image x , namely, $F_{Y \rightarrow X}(G_{X \rightarrow Y}(x)) \rightarrow x$. Similarly, it can bring an image y from class Y back to the original image y , namely, $G_{X \rightarrow Y}(F_{Y \rightarrow X}(y)) \rightarrow y$. Therefore, the cycle consistency loss function of a CycleGAN model is defined as follows:

$$L_{cyc} = F_{Y \rightarrow X}(G_{X \rightarrow Y}(x)) - x + G_{X \rightarrow Y}(F_{Y \rightarrow X}(y)) - y$$

Finally, the full objective function of the CycleGAN model is:

$$\begin{aligned} L(G_{X \rightarrow Y}, F_{Y \rightarrow X}, D_X, D_Y) &= L_{GAN}(G_{X \rightarrow Y}, D_Y, X, Y) \\ &\quad + L_{GAN}(F_{Y \rightarrow X}, D_X, Y, X) + \lambda \cdot L_{cyc} \end{aligned}$$

where λ is a tunable coefficient that controls the importance of the cycle-consistency loss. Detailed explanations of the adversarial loss functions $L_{GAN}(G_{X \rightarrow Y}, D_Y, X, Y)$ and $L_{GAN}(F_{Y \rightarrow X}, D_X, Y, X)$ are described in the original paper on CycleGAN [27]. The training process can be expressed as a min-max optimization of the function

$$\text{Min}_{G_{target}, F_{target}} \text{Max}_{G_{X \rightarrow Y}, F_{Y \rightarrow X}, D_Y, D_Y} L(G_{X \rightarrow Y}, F_{Y \rightarrow X}, D_X, D_Y)$$

Here, generators and discriminators are trained alternatively in a single iteration by fixing of the parameters of the generators during the training process for discriminators and fixing of the parameters of the discriminators during the training process for generators. CycleGAN requires only an unpaired dataset from two image classes, X and Y . Previous studies demonstrated that CycleGAN works well with small datasets in medical domains [23,29,30].

After training, the CycleGAN model learns the characteristic features of both the shallow and deep ACD classes. Therefore, the difference between the original shallow ACD image and the transferred deep ACD image indicates the relative characteristic features of a shallow ACD and vice versa. Image subtraction was performed to obtain the difference between images. By adopting Otsu classic thresholding algorithm, the subtracted image was binarized to visualize the detailed characteristic features of the fundus photograph. Because the attributes of the classes are subtle, thresholding is required to visualize the image features. In a previous study, Otsu thresholding effectively performed segmentation tasks using fundus photographs [31]. For example, a feature map I_{Sub}^Y is generated from a fundus photograph with a shallow ACD y , as follows:

$$I_{Sub}^Y = T_{Otsu}(y - F_{Y \rightarrow X}(y))$$

where T_{Otsu} is Otsu thresholding algorithm. We applied this automated thresholding method to enhance the subtle geometrical features and suppress unwanted noise.

The chronologically split training and test datasets were also used for the development and validation of CycleGAN-based feature map generation. The fundus photograph datasets from a Google Drive account were loaded to the CoLaboratory's environment. We used the CoLaboratory's CycleGAN tutorial page to develop and validate the CycleGAN model, and all these codes are available on the Tensorflow webpage (<https://www.tensorflow.org/tutorials/generative/cyclegan>). We only modified the input pipeline to import our dataset and did not adjust the networks and parameters.

2.5. Statistical analysis & model evaluation

To evaluate the performance of the developed deep learning model, we calculated the areas under the receiver operating characteristic curve (AUCs) for predicting the presence of a shallow ACD (ACD ≤ 2.80 mm and ≤ 2.60 mm). The AUCs were compared using the Delong method provided by MedCalc 20 (MedCalc, Mariakerke, Belgium). Youden's index, a widely used estimate of the

optimal threshold that gives equal weight to sensitivity and specificity, was adopted in this study. The performance metrics for this analysis are expressed as follows:

$$\text{Accuracy} = \frac{TP + TN}{TP + TN + FP + FN}$$

$$\text{Sensitivity} = \frac{TP}{TP + FN}$$

$$\text{Specificity} = \frac{TN}{TN + FP}$$

$$\text{Youden index} = \text{Sensitivity} + \text{Specificity} - 1$$

where TP , TN , FP , and FN denote the numbers of true positives, true negatives, false positives, and false negatives, respectively, in a classification result. Performance was demonstrated using five-fold cross-validation within the training dataset and test dataset validation. To evaluate the ACD prediction performance of the deep learning regression model, we used the metrics of the mean absolute error (MAE) and Pearson correlation coefficient. All statistical tests were performed in a two-sided manner with the significance level of P-value < 0.05 .

To gain insight and interpretability of the final XGBoost model's decision (XGBoost + ResNet50), we calculated the SHapley Additive exPlanations (SHAP) for the patients in the validation dataset. This technique has been used in many ophthalmology data mining tasks, with the selection of informative variables and predicting clinical values with the interpretability of the XGBoost model [32]. The calculated SHAP values were used to create feature importance plots and compare the contributions of fundus photography and clinical variables to predict myopic regression.

The localization experiment was performed using the eyes with pathologically shallow ACD [33,34], to evaluate the CycleGAN-based feature map. The pathologies in the fundus photographs were labeled according to a board-certified ophthalmologist. The localization results were compared with the CycleGAN-based feature maps and the heatmaps of Grad-CAM, guided grad-CAM, and local interpretable model-agnostic explanations (LIME) [35].

GAN-based data augmentation methods have recently been used for ophthalmology imaging domains [36]. Additional experiments using CycleGAN [30], DCGAN [37], PGGAN [38], and SPA-GAN [39] were conducted to investigate whether they could avoid overfitting and improve performance. We cannot use supervised learning-based GAN techniques such as pix2pix because they need annotation for each image [40]. Synthetic images were generated via GAN using an initial training set for augmentation, and they were used to train the classification models.

2.6. Data availability

The datasets are not redistributable to researchers other than those engaged in research collaborations with the B&VIIT Eye Center, South Korea, with the approval of the Institutional Review Board. The datasets utilized in this study are not publicly available because of reasonable privacy and security concerns. Instead, a sample of anonymized fundus photography data with shallow and deep ACD is available from a publicly accessible source (<https://data.mendeley.com/datasets/zz768t4fs5>). Note that this was not the exact data used in the research, rather, it was a cleaned-up reproduction of our study's key insight.

3. Results

We trained the deep learning model to predict a shallow ACD and tested it using a prospective validation design. The clinical

Table 1
Subjects' characteristics in the training and test validation datasets.

	Total	Training set	Test set	P-value*
Number of subjects	891	594	297	
Number of eyes	1782	1188	594	
Clinical variables				
Age at visit (years)	30.94 ± 6.25	30.97 ± 6.27	30.88 ± 6.21	0.778
Sex, number of subjects (%), female)	1236 (69.3)	836 (70.3)	400 (67.3)	0.210
Refractive error (mean SE, Diopters)	-5.21 ± 2.39	-5.28 ± 2.44	-5.08 ± 2.29	0.080
Intraocular pressure (mmHg)	15.44 ± 2.67	15.43 ± 2.63	15.44 ± 2.75	0.990
Central corneal thickness (μm)	538.6 ± 31.6	539.25 ± 30.60	537.36 ± 33.55	0.234
Target measurements				
ACD (mm)	3.21 ± 0.26	3.21 ± 0.25	3.21 ± 0.26	0.941
Number of ACD ≤ 2.60 mm (%)	30 (1.7)	19 (1.6)	11 (1.9)	0.415
Number of ACD ≤ 2.80 mm (%)	119 (6.7)	72 (6.1)	47 (7.9)	0.086

Data are presented as mean ± standard deviation unless noted otherwise.

ACD, anterior chamber depth; SE, spherical equivalent.

*Comparison of training and test sets.

Table 2

Multivariable logistic regression and receiver operating characteristics curve analysis of the prediction of a shallow anterior chamber depth (2.80 mm or lower) using clinical variables in the training dataset.

Clinical variables	Multivariable logistic regression			ROC (for single-parameters)	
	Beta coefficient	Odd ratio (95% CI)	P-value	AUC (95% CI)	P-value
Age (year)	0.083	1.09 (1.05–1.13)	<0.001	0.638 (0.571–0.705)	<0.001
Sex (0: male, 1: female)	0.109	1.12 (0.87–1.42)	0.384	0.545 (0.477–0.612)	0.216
Refractive error (Spherical equivalent, D)	-0.090	0.91 (0.80–1.04)	0.177	0.450 (0.378–0.521)	0.162
Intraocular pressure (mmHg)	0.080	1.08 (0.97–1.21)	0.150	0.531 (0.462–0.600)	0.395
Central corneal thickness (μm)	-0.001	1.00 (0.99–1.01)	0.851	0.503 (0.431–0.576)	0.928

AUC, area under curve; CI, confidence interval; ROC, receiver operating characteristic curves.

characteristics of the study subjects are summarized in **Table 1**. We found no significant differences in the distribution of clinical variables between the training and validation datasets. The subjects had a mean age of 30.94 years and a mean ACD of 3.21 mm in the total dataset. Eyes with shallow ACD (≤ 2.80 mm) were rare. There were 81 eyes (6.8%) in the training and 42 eyes (7.1%) in the test datasets. The odd ratios and prediction results for predicting shallow ACD using clinical variables including age, sex, spherical equivalent, IOP, and center corneal thickness from the training dataset are shown in **Table 2**. Age is the most significant single-parameters to classify shallow ACD in the multivariable logistic regression (P -value < 0.001) and ROC analysis (AUC, 0.638; [95% confidence interval [95% CI], 0.571–0.705]; P -value < 0.001).

Table 3 shows the performance of the shallow ACD detection in five-fold cross-validation using the training dataset. In predicting a shallow ACD with 2.60 mm or lower, the combined model integrating clinical variables and fundus photographs (XGBoost + ResNet50) achieved an AUC of 0.952 (95% CI, 0.939–0.964), and outperformed the machine learning models using only clinical variables (logistic regression, FFANN, and XGBoost; P -value <0.0001 for all comparisons) and deep learning models using only fundus photographs (EfficientNet-B0, DarkNet-53, and ResNet50; P -value <0.05 for all comparisons). The best model (XGBoost + ResNet50) using all factors and fundus photography yielded an accuracy of 89.3% (95% CI, 87.4–91.0%), sensitivity of 94.7% (95% CI, 74.0–99.9%), and specificity of 89.2% (95% CI, 87.3–90.9%). In predicting shallow ACD with 2.80 mm or less, the combined model integrating clinical variables and fundus photographs (XGBoost + ResNet50) achieved an AUC of 0.891 (95% CI, 0.872–0.909), accuracy of 81.8% (95% CI, 79.5–83.9%), sensitivity of 84.7% (95% CI, 74.3–92.1%), and specificity of 81.6% (95% CI, 79.2–83.9%). The performance of this model (XGBoost + ResNet50) was better than that of the machine learning models using only clinical variables (logistic regression, FFANN, and XGBoost; P -value <0.0001 for all comparisons) and deep learning models using only fundus photographs (EfficientNet-B0, DarkNet-53, and ResNet50; P -value <0.05 for all comparisons).

value <0.0001 for all comparisons). The combined XGBoost (XGBoost + ResNet50) and FFANN (FFANN + ResNet50) did not show the difference of integrating clinical variables and fundus photography for predicting a shallow ACD with 2.60 mm or lower (P -value = 0.5166) and a shallow ACD with 2.80 mm or less (P -value = 0.1522).

Table 4 lists the performances of the classification models in the test dataset validation. For predicting both a shallow ACD with 2.60 mm or lower and a shallow ACD with 2.80 mm or lower, the combined model using clinical variables and fundus photography (XGBoost + ResNet50) showed a significantly better AUC than the models using only clinical variables (logistic regression, FFANN, and XGBoost; P -value <0.05 for all comparisons) and deep learning models using only fundus photographs (EfficientNet-B0, DarkNet-53, and ResNet50; P -value <0.05 for all comparisons) in the validation on the test dataset. **Fig. 8** presents the corresponding receiver operating characteristic curves for individual prediction results. For predicting a shallow ACD with 2.60 mm or less, the AUC of the logistic regression using only clinical variables was 0.776 (95% CI, 0.741–0.809), the ResNet50 model using only fundus photographs had an AUC of 0.941 (95% CI, 0.919–0.959), while the combined model integrating clinical variables and fundus photographs (XGBoost + ResNet50) had an AUC of 0.978 (95% CI, 0.963–0.988). The best model (XGBoost + ResNet50) achieved an accuracy of 94.3% (95% CI, 92.1–96.0%), sensitivity of 90.9% (95% CI, 58.7–99.8%), and specificity of 94.3% (95% CI, 92.1 – 96.1%). For predicting a shallow ACD with 2.80 mm or less, the combined model integrating clinical variables and fundus photographs (XGBoost + ResNet50) achieved an AUC of 0.895 (95% CI, 0.868–0.919), outperforming the logistic regression model using only clinical variables (AUC=0.664 [95% CI, 0.625–0.702] and ResNet50 model using only fundus photographs (AUC=0.812 [95% CI, 0.779–0.843]). The deep model using all factors predicted shallow ACD with an accuracy of 83.0% (95% CI, 79.7–85.9%), sensitivity of 78.7% (95% CI, 64.3–89.3%), and specificity of 83.4% (95% CI, 79.9–86.4%).

Table 3Performance of machine learning models for detecting a shallow anterior chamber depth in the development dataset ($n = 1188$ eyes) via five-fold cross-validation.

	ROC-AUC (95% CI)	Accuracy (%) (95% CI)	Sensitivity (%) (95% CI)	Specificity (%) (95% CI)	P-value*
Detection of ACD ≤ 2.60 mm					
(A) Models using clinical variables					
Logistic regression	0.709 (0.683–0.735)	53.9 (51.0–56.7)	84.2 (60.4–96.6)	53.4 (50.5–56.3)	<0.0001
One-hidden-layer FFANN	0.721 (0.694–0.746)	60.0 (57.2–62.8)	78.9 (54.4–93.9)	59.7 (56.8–62.5)	<0.0001
XGBoost	0.729 (0.702–0.753)	54.9 (52.0–57.7)	94.7 (73.9–99.9)	54.2 (51.3–57.1)	<0.0001
(B) DL using FP					
EfficientNet-B0	0.881 (0.861–0.898)	85.4 (83.3–87.4)	73.7 (48.8–90.9)	85.6 (83.5–87.6)	0.0225
DarkNet-53	0.881 (0.861–0.899)	71.9 (69.2–74.4)	89.5 (66.9–98.7)	71.6 (68.9–74.2)	0.0242
ResNet50	0.882 (0.862–0.900)	87.4 (85.4–89.2)	78.9 (54.4–93.9)	87.5 (85.5–89.4)	0.0369
(A + B) Clinical variables + FP					
FFANN + ResNet50	0.948 (0.935–0.960)	83.4 (81.2–85.5)	100.0 (82.4–100.0)	83.2 (80.9–85.3)	0.5166
XGBoost + ResNet50	0.952 (0.939–0.964)	89.3 (87.4–91.0)	94.7 (74.0–99.9)	89.2 (87.3–90.9)	Reference
Detection of ACD ≤ 2.80 mm					
(A) Models using clinical variables					
Logistic regression	0.654 (0.626–0.681)	60.5 (57.7–63.3)	65.3 (53.1–76.1)	60.2 (57.3–63.1)	<0.0001
One-hidden-layer FFANN	0.679 (0.652–0.705)	70.3 (67.6–72.9)	59.7 (47.5–71.1)	71.0 (68.2–73.6)	<0.0001
XGBoost	0.679 (0.652–0.705)	61.5 (58.6–64.2)	66.7 (54.6–77.3)	61.1 (58.2–64.0)	<0.0001
(B) DL using FP					
EfficientNet-B0	0.814 (0.791–0.836)	71.0 (68.4–73.6)	80.6 (69.5–88.9)	70.4 (67.7–73.1)	<0.0001
DarkNet-53	0.831 (0.808–0.852)	74.0 (71.4–76.5)	83.3 (72.7–91.1)	73.4 (70.7–75.9)	<0.0001
ResNet50	0.833 (0.811–0.854)	78.4 (75.9–80.7)	73.6 (61.9–83.3)	78.7 (76.2–81.0)	<0.0001
(A + B) Clinical variables + FP					
FFANN + ResNet50	0.883 (0.863–0.901)	78.3 (75.8–80.6)	86.1 (75.9–93.1)	77.8 (75.2–80.2)	0.1522
XGBoost + ResNet50	0.891 (0.872–0.909)	81.8 (79.5–83.9)	84.7 (74.3–92.1)	81.6 (79.2–83.9)	Reference

ACD, anterior chamber depth; AUC, area under the curve; CI, confidence interval; DL, deep learning; FFANN, one-hidden-layer feed-forward artificial neural network; FP, fundus photography; ROC, the receiver operating characteristic curve.

*Comparison of receiver operating characteristic curves with the single best technique (deep learning using all factors) according to the Delong test.

Table 4Performance of machine learning models for detecting a shallow anterior chamber depth in the test dataset ($n = 594$ eyes) via test validation.

	ROC-AUC (95% CI)	Accuracy (%) (95% CI)	Sensitivity (%) (95% CI)	Specificity (%) (95% CI)	P-value*
Detection of ACD ≤ 2.60 mm					
(A) Models using clinical variables					
Logistic regression	0.776 (0.741–0.809)	86.2 (86.2–88.9)	63.6 (30.8–89.1)	86.6 (83.6–89.3)	0.0092
FFANN	0.776 (0.741–0.809)	77.4 (73.9–80.7)	72.7 (39.0–94.0)	77.5 (73.9–80.9)	0.0125
XGBoost	0.777 (0.742–0.810)	90.7 (88.1–92.9)	63.6 (30.8–89.1)	91.25 (88.7–93.4)	0.0117
(B) DL using FP					
EfficientNet-B0	0.938 (0.916–0.956)	82.3 (79.0–85.3)	100.0 (71.5–100.0)	82.0 (78.6–85.0)	0.0230
DarkNet-53	0.935 (0.912–0.953)	84.3 (81.2–87.2)	100.0 (71.5–100.0)	84.1 (80.8–86.9)	0.0191
ResNet50	0.941 (0.919–0.959)	85.4 (82.3–88.1)	90.91 (58.7–99.8)	85.2 (82.1–88.0)	0.0357
(A + B) Clinical variables + FP					
FFANN + ResNet50	0.977 (0.962–0.988)	89.1 (86.3–91.5)	100.0 (71.5–100.0)	88.9 (86.0–91.3)	0.7504
XGBoost + ResNet50	0.978 (0.963–0.988)	94.3 (92.1–96.0)	90.9 (58.7–99.8)	94.3 (92.1–96.1)	Reference
Detection of ACD ≤ 2.80 mm					
(A) Models using clinical variables					
Logistic regression	0.664 (0.625–0.702)	55.2 (51.1–59.3)	74.5 (59.6–86.1)	53.6 (49.3–57.8)	<0.0001
FFANN	0.661 (0.621–0.699)	52.5 (48.4–56.6)	76.6 (61.9–87.7)	50.5 (46.2–54.7)	<0.0001
XGBoost	0.677 (0.637–0.714)	59.6 (55.5–63.6)	72.3 (57.4–84.4)	58.5 (54.2–62.7)	<0.0001
(B) DL using FP					
EfficientNet-B0	0.810 (0.776–0.841)	80.8 (77.4–83.9)	72.3 (57.4–84.4)	81.5 (78.0–84.7)	0.0006
DarkNet-53	0.812 (0.779–0.843)	74.4 (70.7–77.9)	78.7 (64.3–89.3)	74.0 (70.2–77.7)	0.0012
ResNet50	0.812 (0.779–0.843)	76.8 (73.2–80.1)	85.1 (71.7–93.8)	76.1 (72.3–79.6)	0.0012
(A + B) Clinical variables + FP					
FFANN + ResNet50	0.894 (0.866–0.917)	79.6 (76.2–82.8)	80.9 (66.7–90.9)	79.5 (75.9–82.8)	0.8488
XGBoost + ResNet50	0.895 (0.868–0.919)	83.0 (79.7–85.9)	78.7 (64.3–89.3)	83.4 (79.9–86.4)	Reference

ACD, anterior chamber depth; AUC, area under the curve; CI, confidence interval; DL, deep learning; FFANN, one-hidden-layer feed-forward artificial neural network; FP, fundus photography; ROC, the receiver operating characteristic curve.

* Comparison of receiver operating characteristic curves with the single best technique (deep learning using all factors) according to the Delong test.

Fig. 9 shows the importance of the features in the final combined model (XGBoost + ResNet50). The ResNet50 outcome using fundus photography was more important than other variables, including age, sex, refractive error, IOP, and central corneal thickness, to predict both shallow ACD with 2.60 mm or lower and shallow ACD with 2.80 mm or lower. **Fig. 10** shows examples of the results from the developed model predicting the deep and shallow ACD with saliency maps using Grad-CAM. The saliency maps show that the deep learning model generally uses the features of relatively peripheral regions around the macula to predict deep ACD

and the foveal area to predict shallow ACD. The heatmaps provided by Grad-CAM highlight wide salient regions but are unable to specify which shape or structure of the retina are involved in predicting for both classes. The characteristic features of shallow and deep ACD in the fundus photographs are not detected in the saliency maps.

The CycleGAN-based feature maps for shallow ACD were quite different from the heatmaps from Grad-CAM, as shown in **Fig. 11**. The changes in image translation by the generators of CycleGAN were difficult to detect with the naked eye. However, image sub-

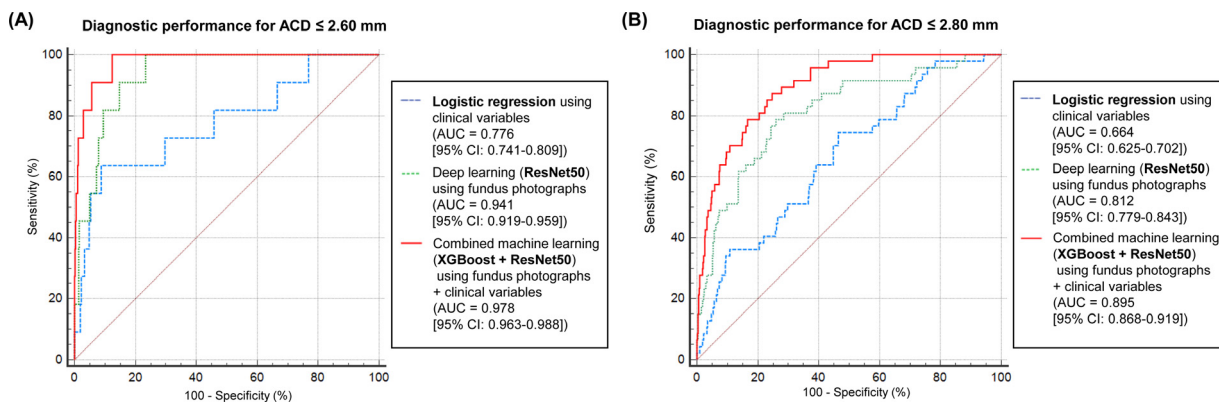


Fig. 8. Classification performance of logistic regression and deep learning models for detecting shallow anterior chamber depth (ACD) in the test dataset validation. Receiver operating characteristic curves for (A) a shallow ACD with 2.60 mm or less and (B) a shallow ACD with 2.80 mm or less.

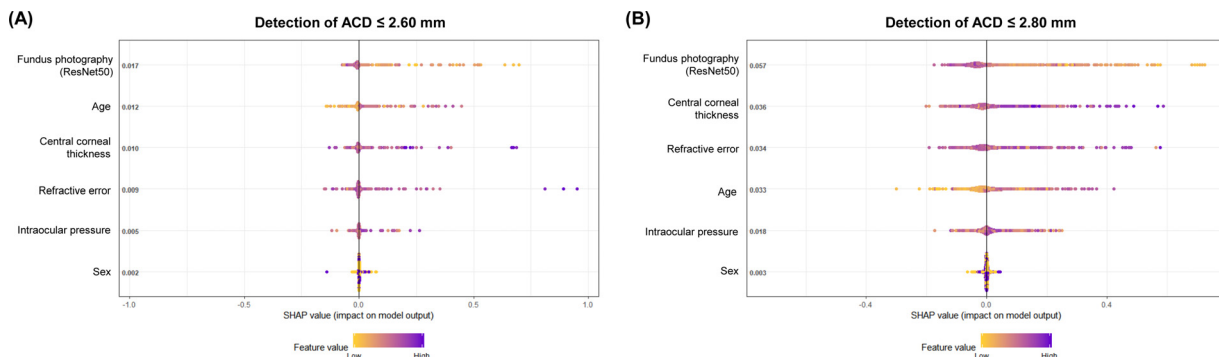


Fig. 9. SHAP plots represent the importance of features and the contribution of input variables to the XGBoost integration in the combined model (XGBoost + ResNet50). Feature importance from the test validation dataset for detecting (A) a shallow ACD with 2.60 mm or less and (B) a shallow ACD with 2.80 mm or less. The features include the softmax function outcome of the ResNet50 model using fundus photography, age, sex, refractive error, intraocular pressure, and central corneal thickness. SHAP, SHapley Additive exPlanations.

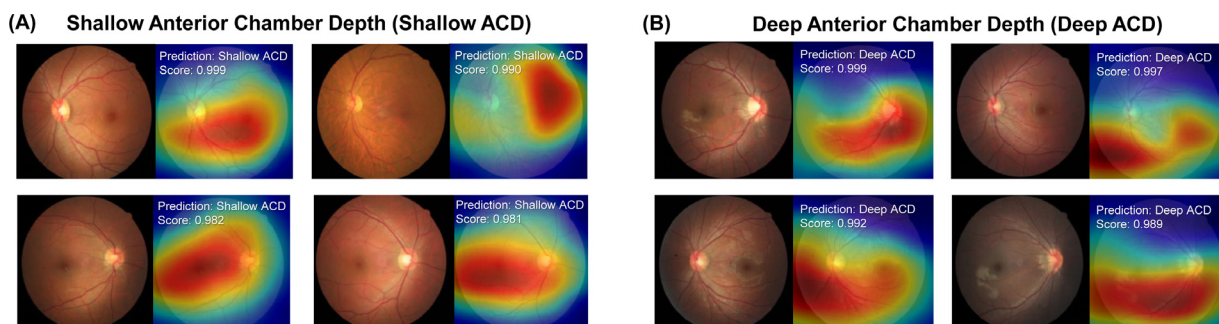


Fig. 10. Examples of the developed deep learning results with a saliency map using the Grad-CAM technique. Original fundus photographs and heatmaps of the deep learning model for predicting a (A) shallow or (B) deep anterior chamber depth (ACD).

traction and Otsu thresholding techniques successfully visualized the feature changes of fundus photographs for shallow ACD. According to the average image of the feature maps from the test dataset, the characteristic feature maps show that the brightened area surrounding the macula and optic disk is more closely associated with a shallow ACD than a deep ACD. This CycleGAN-based feature map visualizes more specific patterns of a shallow ACD with finer resolutions than the saliency map from Grad-CAM. Fig. 12 presents the feature maps for the deep ACD generated by the CycleGAN. On the average image, we observed that the macular area in the fundus photographs was associated with a deep ACD. The saliency maps based on Grad-CAM commonly outline the area where the brightness changes rapidly compared with the CycleGAN-based feature maps. Fig. 13 shows that the CycleGAN-

based feature map change according to ACD measurement. Images generated from a shallow ACD ($ACD \leq 2.60$ mm) exhibits a more apparent pattern than a less shallow ACD ($ACD \leq 2.80$ mm). Fig. 14 compares visualization methods for explaining deep learning results in various cases. The CycleGAN-based feature map shows the patterns across the whole fundus photographs, while the Grad-CAM, guided Grad-CAM, and LIME focused on only local parts.

Additionally, we evaluated the gap between AI-based localization and human expert annotation for predicting pathologically shallow ACD, as shown in Fig. 15. The expert frequently annotated macular folds, optic disk, and hazy areas due to cataracts because these pathologies are associated with a shallow ACD. The CycleGAN-based feature maps highlighted similar areas for predict-

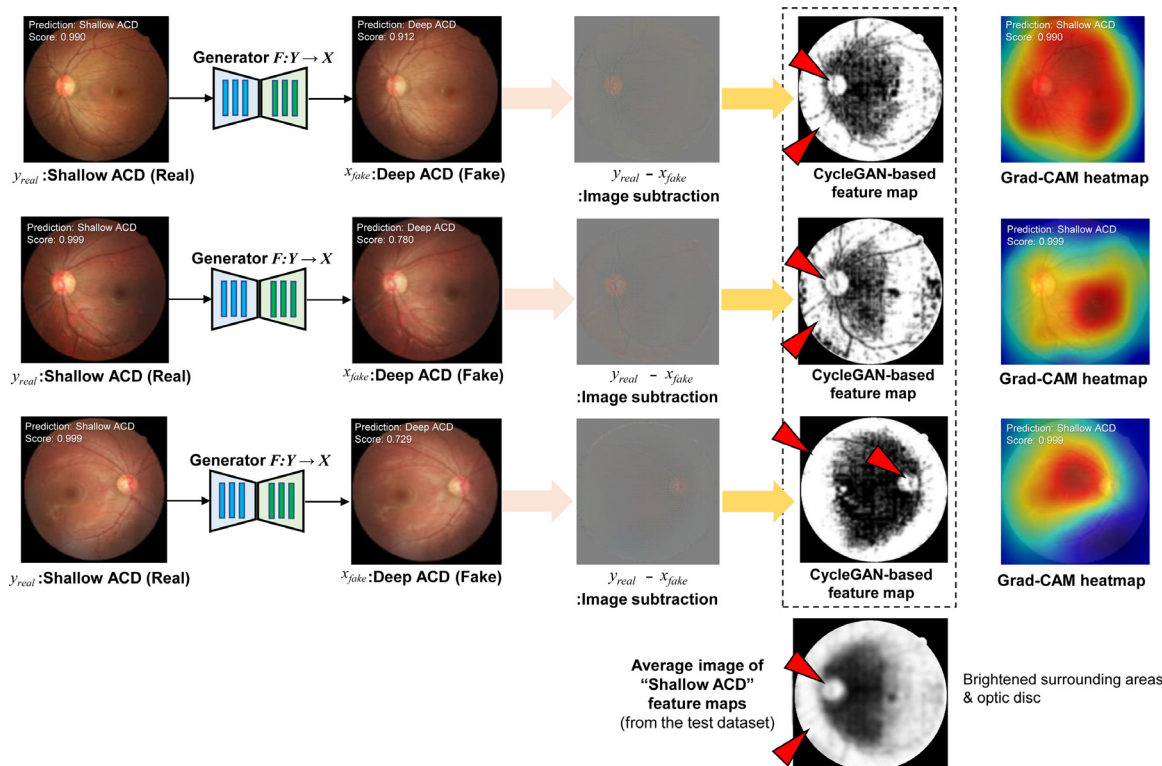


Fig. 11. Examples of the CycleGAN-based feature images for shallow anterior chamber (ACD) detection on fundus photographs. CycleGAN-based feature maps generation processes and corresponding saliency maps from the test dataset. The red arrows highlight the area surrounding the macula and optic disk in the CycleGAN-based feature maps.

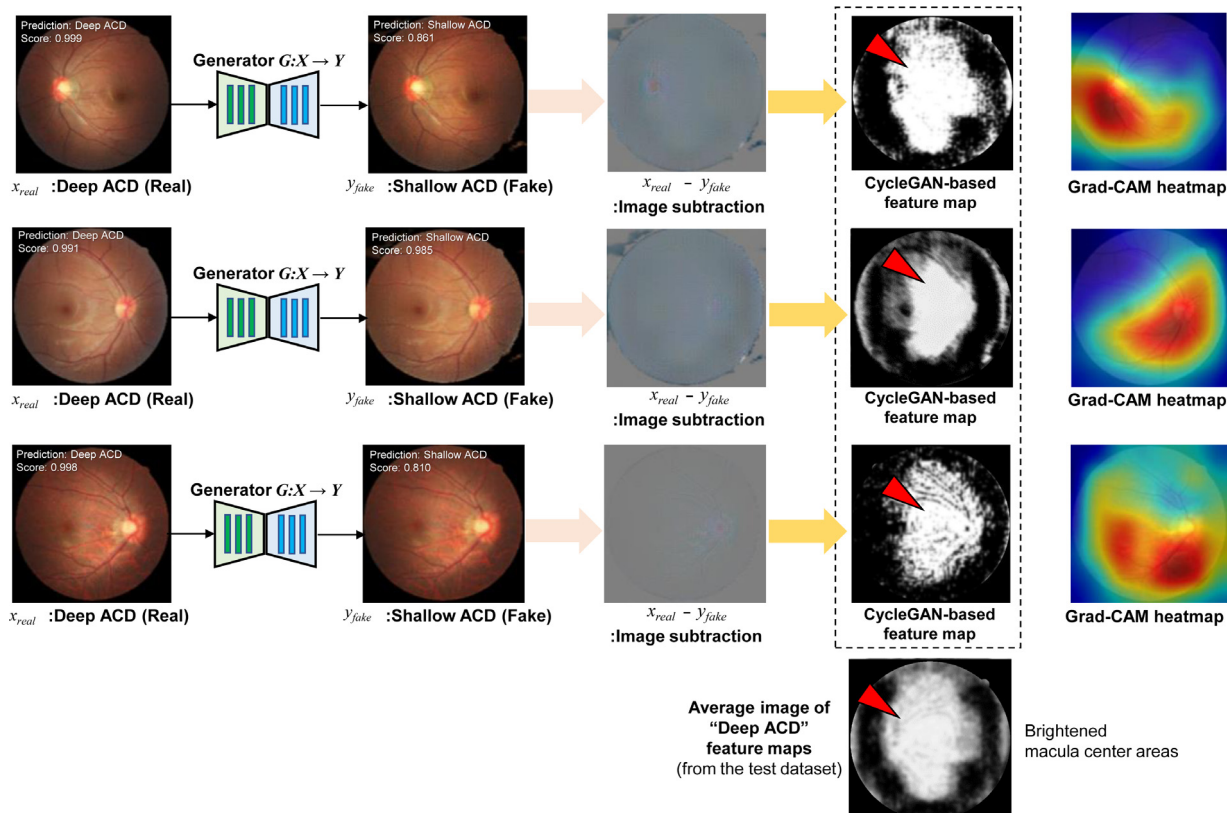


Fig. 12. Examples of the CycleGAN-based feature images for deep anterior chamber (ACD) detection using fundus photographs. CycleGAN-based feature maps generation processes and corresponding saliency maps from the test dataset. The red arrows highlight the macular areas in the CycleGAN-based feature maps.

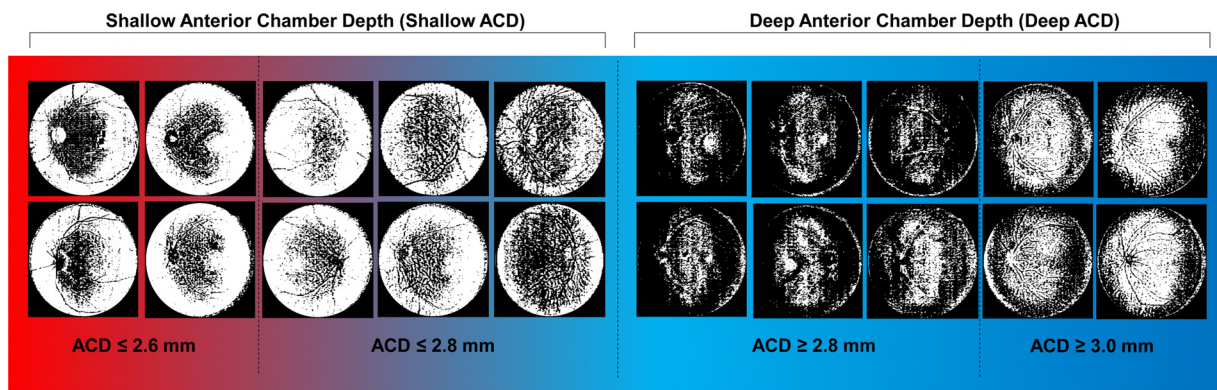


Fig. 13. Examples present the CycleGAN-based feature maps of shallow and deep anterior chamber (ACD) classes.

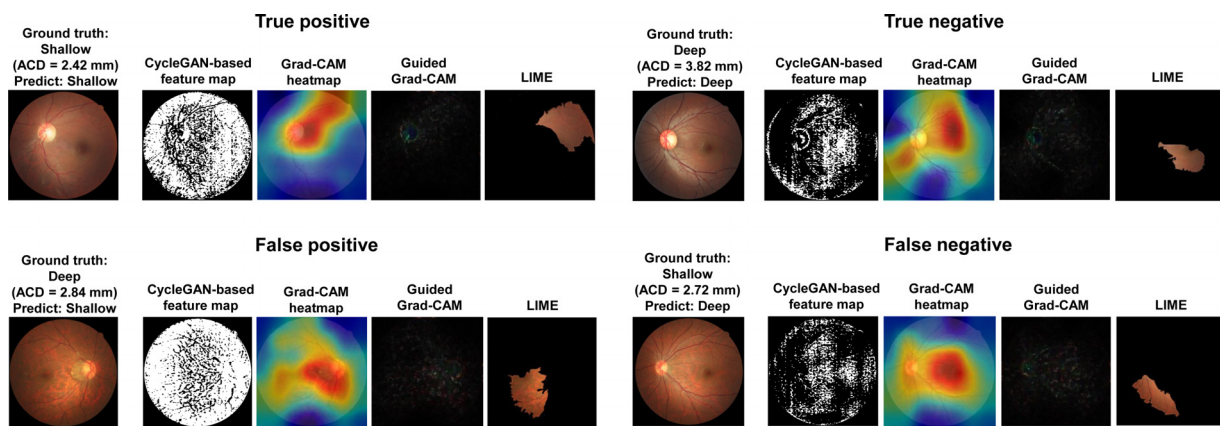


Fig. 14. Comparison of visualization methods for explaining deep learning results in various cases.

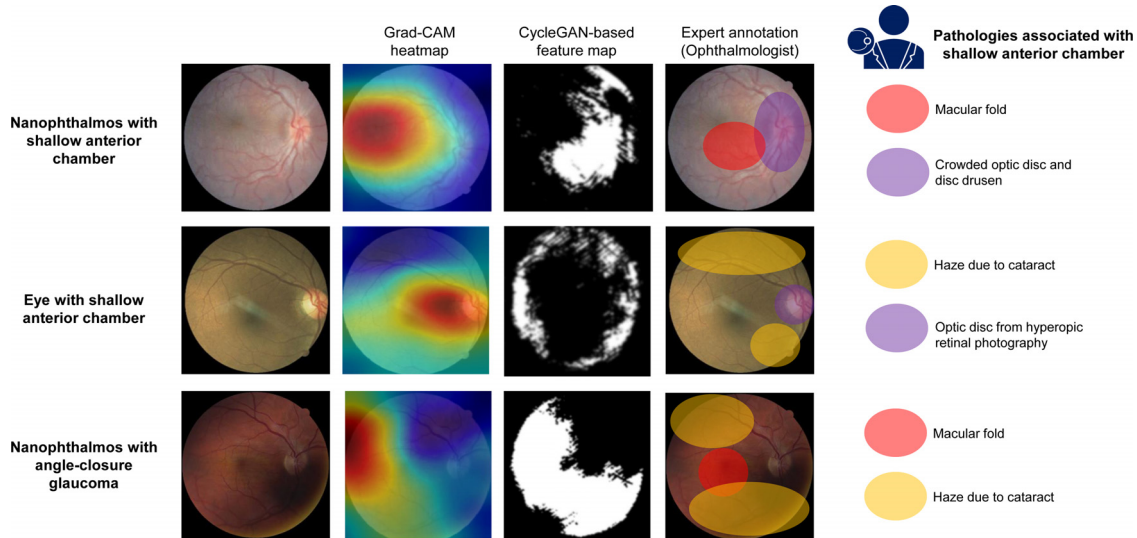


Fig. 15. Additional examples presenting the gaps between artificial intelligence-based lesion localization and expert annotation. The cases include nanophthalmos and normal sized eye with shallow anterior chamber.

ing a shallow ACD. However, Grad-CAM frequently highlighted area where annotated pathologies were not present.

To evaluate whether CNN size affects the performance of predicting a shallow ACD, we compared the performances of ResNet18, ResNet50 (as a reference), ResNet101, and InceptionResNetV2 in the test dataset (Table 5). There were no statistical differences in the models' AUC of prediction performance. Table 6

shows the results for GAN-based data augmentation to predict a shallow ACD. The CycleGAN-based augmentation shows better improvement than other techniques but the gain of augmentation was relatively small (+2.7% for detection of $ACD \leq 2.60$ mm and +2.0% for detection of $ACD \leq 2.80$ mm).

We also evaluated the CycleGAN-based feature map generation in the diabetic retinopathy dataset using a publicly accessi-

Table 5

Classification performance via test dataset validation of deep learning models based on the ResNet architecture.

	Backbone convolutional neural network architecture (DL using only fundus photography)			
	ResNet18	ResNet50	ResNet101	InceptionResNetV2
Depth	18	50	101	164
Parameters (millions)	11.7	25.6	44.6	55.9
Detection of ACD \leq 2.60 mm				
ROC-AUC (95% CI)	0.936 (0.913–0.954)	0.941 (0.919–0.959)	0.945 (0.923–0.962)	0.939 (0.916–0.957)
P-value	0.7513	Reference	0.8062	0.8485
Detection of ACD \leq 2.80 mm				
ROC-AUC (95% CI)	0.816 (0.782–0.846)	0.812 (0.779–0.843)	0.797 (0.762–0.828)	0.781 (0.745–0.813)
P-value	0.9252	Reference	0.6851	0.3507

ACD, anterior chamber depth; AUC, area under the curve; CI, confidence interval; DL, deep learning; ROC, receiver operating characteristic curve.

Table 6

Comparison of data augmentation techniques based on generative adversarial networks to predict shallow anterior chamber depth in the test dataset ($n = 594$ eyes) via test validation.

Augmentation technique	Setting for minor class (real vs synthetic ratio)	Detection of ACD \leq 2.60 mm*		Detection of ACD \leq 2.80 mm*	
		Accuracy (%)	Improvement (%)	Accuracy (%)	Improvement (%)
CycleGAN† [30]	Deep ACD (randomly selected) \rightarrow shallow ACD (1:2)	87.1	+2.7	78.8	+2.0
DCGAN [37]	Randomly generated shallow ACD images (1:2)	83.1	-2.3	72.9	-3.9
PGGAN [38]	Deep ACD (randomly selected) \rightarrow shallow ACD (1:2)	85.9	+0.5	78.6	+1.8
SPA-GAN [39]	Randomly generated shallow ACD images (1:2)	86.2	+0.8	77.5	+0.6

ACD, anterior chamber depth; GAN, generative adversarial network.

*ResNet50 performed classification tasks.

†The GAN technique mainly used in our study.

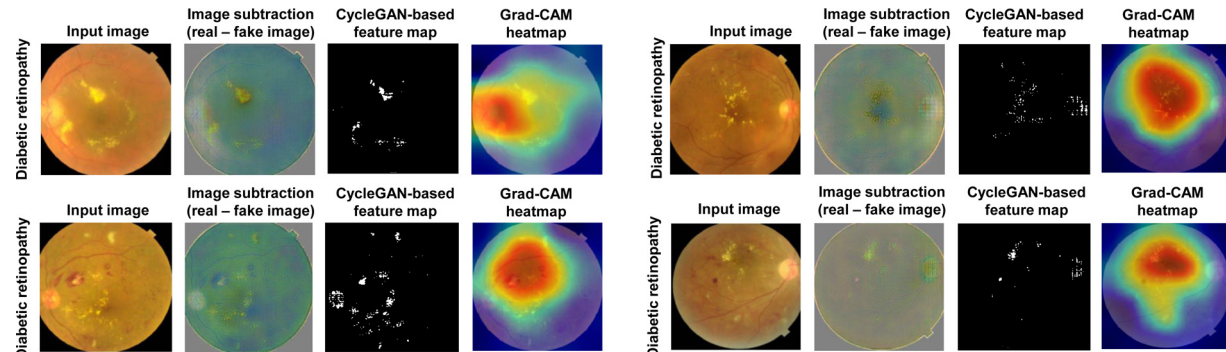


Fig. 16. CycleGAN-based feature map generation in the diabetic retinopathy dataset. We used retinal images from the Retinal Fundus Multi-Disease Image Dataset (RFMiD), which are publicly available. In this experiment, diabetic retinopathy images were mapped into the normal fundus images using CycleGAN.

ble fundus photography dataset [41]. In this experiment, diabetic retinopathy images (source class X) were mapped into the normal fundus images (target class Y) using CycleGAN, and image subtraction and thresholding were performed. Fig. 16 shows that the CycleGAN-based feature maps successfully highlighted pathologies of diabetic retinopathy such as hemorrhages and exudates. However, Grad-CAM failed to indicate the pathology of each disease.

4. Discussion

Here, we introduced deep learning models that determined the risk of a shallow ACD and highlighted the characteristic hidden features of fundus photographs. The proposed CycleGAN-based feature map can show the characteristic features of shallow ACD on fundus photographs that cannot be detected using a conventional explainable AI technique. We also found that adding several clinical variables to the deep learning model can improve its diagnostic performance. This shows that information fusion with multiple sources and fundus photography can achieve smarter retinal image screening for a shallow ACD that is undetectable by ophthalmologists. This prediction of shallow ACD using fundus photographs has never been carried out by both ophthalmologists and AI re-

searchers, indicating the development of novel medical AI to aid in clinical screening and diagnosis. We also demonstrated that the proposed CycleGAN-based feature map can visualize the hidden characteristic features of the target class. This technique is similar to the GAN-based explanation that was proposed to improve the saliency map [28], but we significantly improved the existing method to visualize more clearly with simple Otsu thresholding method and applied it to a real medical problem. Using this framework, we discovered that novel patterns on fundus photographs are associated with a shallow ACD. Therefore, this study has significant advantages compared to previous deep learning studies of the detection of shallow ACD from other imaging domains (Table 7).

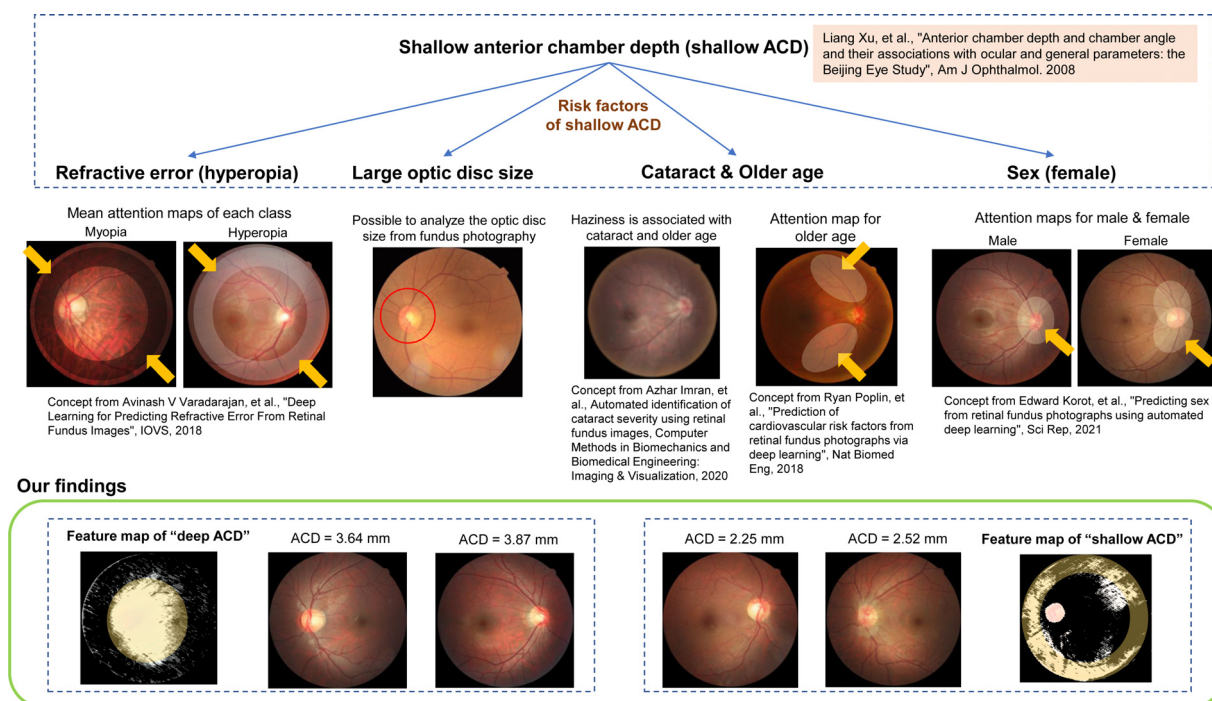
The developed deep learning model achieved good performance at identifying shallow ACD in this study. According to the feature map generated by CycleGAN and the thresholding method, retinal image patterns may be associated with a shallow ACD. We hypothesize that several risk factors may be detected in the posterior pole of the eye via deep learning, as shown in Fig. 17. In a previous study, a shallow ACD is associated with age, sex, refractive error, cataract, and optic disk size [42]. Cataracts, older age, and sex differences have been reported as factors on fundus photographs detectable by deep learning [14,43]. According to a pre-

Table 7

Summary of the deep-learning-based techniques for angle-closure glaucoma or shallow anterior chamber depth detection in ophthalmology image domains.

Study	Algorithm	Image domain	Summary
Fu, et al. 2019 [9]	VGG16	Anterior segment optical coherence tomography	The deep learning system showed an AUC of 0.90 for angle-closure detection in the cross-sectional images of the anterior segment.
Xu, et al. 2019 [58]	ResNet18	Anterior segment optical coherence tomography	Deep learning classifiers detected gonioscopic angle closure and primary angle-closure glaucoma with an AUC of 0.933.
Fu, et al. 2019 [59]	Multi-level deep network	Anterior segment optical coherence tomography	The multilevel deep learning was adopted for analyzing three particular parts including global anterior segment, structure, local iris region, and anterior chamber angle patches and showed better performance than other methods.
Wang, et al. 2021 [60]	EfficientNet-B3 and U-Net	Ultrasound biomicroscopy (UBM)	The deep learning system realized the automatic measurement of the angle parameters such as anterior chamber angle, trabecular-iris angle, and angle-opening distance.
Qian, et al. 2021 [61]	InceptionV3	Anterior segment photographs from pentacam HR	The deep learning model achieved an AUC of 0.86 for detecting shallow ACD using a high-resolution rotating Scheimpflug camera.
Our study	ResNet50 and CycleGAN	Classic color fundus photographs	The deep learning model integrating fundus photographs and clinical variables achieved an AUC of 0.89. The CycleGAN-based feature images identified the features of shallow ACD.

ACD, anterior chamber depth; AUC, area under the curve.

**Fig. 17. A hypothesis of the association between fundus photographs with a shallow or deep anterior chamber depth (ACD).** Previous deep learning studies have showed that the risk factors, which were previously identified in an epidemiologic study [42], are associated with fundus photography [14,15,44].

vious study, sex differences are generally found in and around the optic disk [44]. Because refractive error can also be estimated using deep learning [15], hyperopia with a shallow ACD can be predicted from fundus photographs. According to the mean attention feature maps in Varadarajan's work [15], we observed that the area surrounding the macula contribute to the detection of hyperopia and differ from the pattern that appears in the detection of myopia. These factors may have significantly contributed to the prediction of a shallow ACD via deep learning in this study. According to our findings, the main pattern may include a slight change in optic nerve size, changes in texture around the macula, and differences in vessel arcade shape. These are hidden patterns on fundus photography because they are subtle and difficult to see with the naked eye. The deep learning model successfully predicted a shallow ACD from fundus photographs that contain much clinical and

optical information and systemic factors using a data-driven technique.

In this study, the hidden features of a shallow ACD were the brightened surroundings of the macula and optic disk, which were difficult to be detected with the naked eye. They were different patterns from pathological lesions such as hemorrhage, exudate, pigmentation, or fluid that could be immediately recognized in the retina. The characteristic hidden features of a shallow ACD on fundus photographs that are undetectable by ophthalmologists are detected and generated through deep learning. To understand the hidden characteristics of fundus photographs with a shallow ACD and overcome the black-box effect of deep learning, we developed a CycleGAN-based visualization technique to demonstrate the differences between shallow and deep ACD on fundus photographs. We observed that GAN-based image-to-image translation methods

Table 8

Comparison between the proposed CycleGAN-based method and other visual explanation techniques.

Visual explanation techniques	Mechanism categories [47]	Strengths	Limitations	Suitability for our ACD dataset	Time complexity – Inference*
ResNet50 + CycleGAN (proposed method)	Feature extraction based on a mathematical structure	Global representation of the features based on data distribution	Decoupled CNN and explainer modules	Good (visualizing global subtle features)	$O(N)$
ResNet50 + Grad-CAM	Decomposition of neural networks	Coupled CNN and explainer modules	Dependent on the strength of CNN activation, not features	Bad (focusing local features)	$O(N)$
ResNet50 + LIME [62]	Evaluation of local feature sensitivity	Showing local image patches / Easy and intuitive concept	Partially coupled CNN and explainer modules / Coarse explanation	Bad (focusing local features)	$O(N) + O(P^2)$
SPA-GAN (CycleGAN + Grad-CAM) [39]	Signal-based optimization + decomposition	Global representation and coupled with CNN	Difficult to train / Needed a large amount of data	Bad (not visualizing subtle features)	$O(N)$

CNN, convolutional neural network; LIME, local interpretable model-agnostic explanations.

*N = image resolution; P = number of image patches.

can provide key features from the input image [28]. Similarly, the CycleGAN-based feature maps provide better explainable features of fundus photographs for each class than the heatmaps provided by Grad-CAM. We found that Grad-CAM commonly highlights a small part of the area in which the brightness changes, but it is not explainable and is undetectable by human users. A previous study demonstrated that Grad-CAM generally performs worse with images of multiple or complex pathological lesions [26]. We demonstrated that the proposed CycleGAN-based technique can generate an explainable feature map that highlights detailed feature areas with finer resolutions. It also shows the direction of pathological feature changes that provide insight into a patient's pathological status. In this study, we observed that fundus photographs with a shallow ACD have a relatively uniform lighting distribution over the retina, and they may never be detected by researchers using Grad-CAM. Since both are based on CycleGAN, our proposed algorithm is similar to SPA-GAN [39]. However, there is a difference that our method extracted intuitive features through subtraction of images without using the activity of the discriminator layer. Considering the image translation to find explainable features, our proposed technique is similar to that in a previous work using an adversarial example [45]. However, adversarial examples were originally developed to perturb images to fool a CNN into making incorrect classifications [46], and the explainable feature images produced by adversarial examples might be noise or perturbation images.

According to the previous study [47], our framework using ResNet50 and CycleGAN-based feature map can be categorized into the feature extraction-based interpretability technique via mathematical structure. Table 8 compares the proposed algorithm with other visual explanation methods. The proposed algorithm has no weakness in the amount of computation in image inference and visualization. CycleGAN takes much time to train, but inference does not require additional operations other than passing through the generator. On the other hand, the LIME method's computation may increase exponentially according to the number of image patches. Other explanation techniques were unsuitable for this study because they were challenging to point to global features or visualize subtle differences.

Our deep learning model has huge potential for application in clinical settings. Because anterior segment OCT directly measures ACD, it is difficult to compare it with the proposed deep learning method that indirectly estimates ACD. As already mentioned, conventional methods to measure ACD, including pentacam and anterior segment OCT, have several disadvantages, such as low reproducibility, bulky equipment, and a time-consuming examination. Because of the widespread availability of fundus photogra-

phy equipment in clinics and check-up centers, the proposed deep learning model can provide an effective screening tool for a shallow ACD, which was previously undetectable using retinal images. Since fundus photography is currently used for large-scale screenings, many cases of a shallow ACD and subsequent ACG will be discovered by our model before the angle-closure attack occurs. Similar to the previous work extending the diagnostic ability of fundus photography, our proposed model can be applied not only to local hospitals but also to remote areas for health screening [48]. Therefore, the development of a deep learning model that uses fundus imaging devices may be cost-effective because it does not require additional equipment. It will also facilitate the early detection of shallow ACD and, therefore, benefit many patients.

There were relatively few patients with pathological conditions in our study. Due to data imbalance, the sensitivity of prediction performance has a wide range of confidence intervals and P-values. This imbalance also affects accuracy a lot, so the accuracy of each model does not accurately reflect the classification ability. We successfully overcame this imbalance problem through conventional data augmentation and transfer learning. Similar to what previous studies have performed [23,49], we tried to perform data augmentation through CycleGAN. In our experiment, the improvement of prediction performance was not significant considering the computation loads of the GAN techniques. A previous study revealed that GAN-based data augmentation may worsen the prediction performance in unseen datasets due to its limited image generation ability [50].

Our work predicted a shallow ACD value by binarizing ACD measurement, although the binarization inevitably causes information loss [51]. Since all the CNN models we used are pre-trained in the ImageNet [52], performance may be limited in each task. Future works should adopt novel deep learning frameworks to improve the prediction performance rather than using classic CNN models. Recently, much progress has been made on binary deep learning networks preserving quantitative information [53]. A spatio-temporal deformable convolutional network module with an attention mechanism could be another solution to learn more accurate pattern recognition for fundus photography [54].

The strength of the current study is the use of a large volume of ACD data, which enabled us to link fundus photographs for shallow ACD detection, although the accuracy of ACD detection is relatively low (83.0% for a shallow ACD with 2.80 mm or lower). However, it has acceptable performance as a predictive model for screening purposes. If screening based on fundus photography detects a person at high-risk of a shallow ACD or ACG, additional examinations such as anterior OCT may be performed to enable a more accurate diagnosis. More pathological data with a shallow ACD will

lead to increased performance of the AI model [30]. Although a shallow ACD is closely associated with ACG, screenings for it are not performed in most clinics. We found that retinal photographs alone provided more information about ACD than clinical variables such as age, refractive error, and IOP. In addition, the concept of CycleGAN-based feature map generation is relatively simple and can provide detailed characteristic feature images of shallow and deep ACD from fundus photographs. We believe that this framework that generates explainable feature images can be extended to the prediction of other clinical imaging domains.

This study has several limitations. First, the datasets consisted of an East Asian population from a single center. A previous study showed that structural parameters measured by anterior segment OCT varied by ethnicity [55]. Therefore, it is unknown whether our method can be used in other ethnic groups. Second, the developed deep learning model was not validated using an independent external dataset. Many factors can affect fundus photograph images, such as product specifications, software, illumination, and inspector skill [56]. Their impact can be evaluated when the algorithm is verified using a variety of external datasets. Third, selection bias in our dataset was unavoidable because the dataset was obtained from a refractive surgery center. Subjects who intend to undergo refractive surgery generally have myopia and no degenerative ocular disease. Therefore, the dataset used in this study may not be representative of the general population. Fourth, the ACG diagnoses were not confirmed in this study. Currently, gonioscopy is the reference standard method for detecting ACG, but it is time-consuming and laborious [57]. It was difficult to conduct gonioscopy in all patients who visited a refractive surgery center. For this reason, we could not develop a deep learning model to directly diagnose ACG. Fifth, the training and validation datasets included a relatively limited number of subjects. In this regard, future research will focus on data collection, and the performance of the deep learning model can be further enhanced using more ACD measurements and fundus photographs.

5. Conclusion

In conclusion, here we demonstrated the feasibility of a novel deep learning model to detect a shallow ACD using fundus photographs as a screening tool for ACG. We also found that fundus photographs contain diagnostic information about shallow ACD, which was previously unknown. This framework will facilitate the early detection of a shallow ACD to prevent overlooking the risks associated with ACG during retinal examinations and health check-ups using fundus photography. Our study showed that deep learning can link the information of the posterior retina to anterior ocular segment, which should be measured using different sensor. This may significantly reduce the costs of shallow ACD screenings and provide an ACG screening tool in areas where anterior segment imaging devices are not readily available. We hope that the developed AI will help reduce the global burden of ACG.

Funding

This research did not receive any specific grant from funding agencies in the public, commercial, or not-for-profit sectors.

Declaration of Competing Interest

Ik Hee Ryu and Jin Kuk Kim are executives of VISUWORKS, Inc., a Korean AI startup providing medical machine learning solutions. Jin Kuk Kim is an executive of the Korea Intelligent Medical Industry Association. These authors received a salary or stock as part of the standard compensation package. The remaining authors declare no conflict of interest.

Supplementary materials

Supplementary material associated with this article can be found, in the online version, at doi:[10.1016/j.cmpb.2022.106735](https://doi.org/10.1016/j.cmpb.2022.106735).

CRediT authorship contribution statement

Tae Keun Yoo: Writing – original draft, Writing – review & editing, Conceptualization, Methodology, Software, Formal analysis. **Ik Hee Ryu:** Conceptualization, Writing – review & editing. **Jin Kuk Kim:** Writing – review & editing, Conceptualization. **In Sik Lee:** Methodology, Data curation. **Hong Kyu Kim:** Data curation, Resources.

References

- [1] R.J. Casson, Anterior chamber depth and primary angle-closure glaucoma: an evolutionary perspective, *Clin. Experiment. Ophthalmol.* 36 (2008) 70–77, doi:[10.1111/j.1442-9071.2008.01672.x](https://doi.org/10.1111/j.1442-9071.2008.01672.x).
- [2] D.T.L. Quek, V.T. Koh, G.S. Tan, S.A. Perera, T.T. Wong, T. Aung, Blindness and long-term progression of visual field defects in chinese patients with primary angle-closure glaucoma, *Am. J. Ophthalmol.* 152 (2011) 463–469, doi:[10.1016/j.ajo.2011.02.023](https://doi.org/10.1016/j.ajo.2011.02.023).
- [3] H.A. Quigley, A.T. Broman, The number of people with glaucoma worldwide in 2010 and 2020, *Br. J. Ophthalmol.* 90 (2006) 262–267, doi:[10.1136/bjo.2005.081224](https://doi.org/10.1136/bjo.2005.081224).
- [4] T. Aung, P.T.K. Chew, Review of recent advancements in the understanding of primary angle-closure glaucoma, *Curr. Opin. Ophthalmol.* 13 (2002) 89–93.
- [5] V.K. Singh Upasna, J. Rana, S. Kumar, A. Singh, K. Singh, An evaluation of intraoperative and postoperative outcomes of phacoemulsification surgery in eyes with shallow anterior chamber, *Indian J. Ophthalmol.* 69 (2021) 1346–1347, doi:[10.4103/ijo.IJO_3483_20](https://doi.org/10.4103/ijo.IJO_3483_20).
- [6] T. Aung, W.P. Nolan, D. Machin, S.K.L. Seah, J. Baasanhu, P.T. Khaw, G.J. Johnson, P.J. Foster, Anterior chamber depth and the risk of primary angle closure in 2 east asian populations, *Arch. Ophthalmol.* 123 (2005) 527–532, doi:[10.1001/archoph.123.4.527](https://doi.org/10.1001/archoph.123.4.527).
- [7] J.-H. Yi, H. Lee, S. Hong, G.J. Seong, S.Y. Kang, K.T. Ma, C.Y. Kim, Anterior chamber measurements by pentacam and AS-OCT in eyes with normal open angles, *Korean J. Ophthalmol.* 22 (2008) 242–245, doi:[10.3341/kjo.2008.22.4.242](https://doi.org/10.3341/kjo.2008.22.4.242).
- [8] J.G. Devereux, P.J. Foster, J. Baasanhu, D. Uranchimeg, P.S. Lee, T. Erdenebeig, D. Machin, G.J. Johnson, P.H. Alsbirk, Anterior chamber depth measurement as a screening tool for primary angle-closure glaucoma in an East Asian population, *Arch. Ophthalmol.* 118 (2000) 257–263, doi:[10.1001/archoph.118.2.257](https://doi.org/10.1001/archoph.118.2.257).
- [9] H. Fu, M. Basaran, Y. Xu, S. Lin, D.W.K. Wong, J. Liu, T.A. Tun, M. Mahesh, S.A. Perera, T. Aung, A deep learning system for automated angle-closure detection in anterior segment optical coherence tomography images, *Am. J. Ophthalmol.* 203 (2019) 37–45, doi:[10.1016/j.ajo.2019.02.028](https://doi.org/10.1016/j.ajo.2019.02.028).
- [10] G. Shi, Z. Jiang, G. Deng, G. Liu, Y. Zong, C. Jiang, Q. Chen, Y. Lu, X. Sun, Automatic classification of anterior chamber angle using ultrasound biomicroscopy and deep learning, *Trans. Vis. Sci. Tech.* 8 (2019) 25–25, doi:[10.1167/tvst.8.4.25](https://doi.org/10.1167/tvst.8.4.25).
- [11] V. Gulshan, L. Peng, M. Coram, M.C. Stumpe, D. Wu, A. Narayanaswamy, S. Venugopalan, K. Widner, T. Madams, J. Cuadros, R. Kim, R. Raman, P.C. Nelson, J.L. Mega, D.R. Webster, Development and validation of a deep learning algorithm for detection of diabetic retinopathy in retinal fundus photographs, *JAMA* 316 (2016) 2402–2410, doi:[10.1001/jama.2016.17216](https://doi.org/10.1001/jama.2016.17216).
- [12] G. Quellec, M. Lamard, P.-H. Conze, P. Massin, B. Cochener, Automatic detection of rare pathologies in fundus photographs using few-shot learning, *Med. Image Anal.* 61 (2020) 101660, doi:[10.1016/j.media.2020.101660](https://doi.org/10.1016/j.media.2020.101660).
- [13] J. Son, J.Y. Shin, H.D. Kim, K.-H. Jung, K.H. Park, S.J. Park, Development and validation of deep learning models for screening multiple abnormal findings in retinal fundus images, *Ophthalmology* 127 (2020) 85–94, doi:[10.1016/j.jophtha.2019.05.029](https://doi.org/10.1016/j.jophtha.2019.05.029).
- [14] R. Poplin, A.V. Varadarajan, K. Blumer, Y. Liu, M.V. McConnell, G.S. Corrado, L. Peng, D.R. Webster, Prediction of cardiovascular risk factors from retinal fundus photographs via deep learning, *Nat. Biomed. Engin.* 2 (2018) 158.
- [15] A.V. Varadarajan, R. Poplin, K. Blumer, C. Angermueller, J. Ledsam, R. Chopra, P.A. Keane, G.S. Corrado, L. Peng, D.R. Webster, Deep learning for predicting refractive error from retinal fundus images, *Invest. Ophthalmol. Vis. Sci.* 59 (2018) 2861–2868, doi:[10.1167/iovs.18-23887](https://doi.org/10.1167/iovs.18-23887).
- [16] K. Ishii, R. Asaoka, T. Omoto, S. Mitaki, Y. Fujino, H. Murata, K. Onoda, A. Nagai, S. Yamaguchi, A. Obana, M. Tanito, Predicting intraocular pressure using systemic variables or fundus photography with deep learning in a health examination cohort, *Sci. Rep.* 11 (2021) 3687, doi:[10.1038/s41598-020-80839-4](https://doi.org/10.1038/s41598-020-80839-4).
- [17] E.M. Kang, I.H. Ryu, G. Lee, J.K. Kim, I.S. Lee, G.H. Jeon, H. Song, K. Kamiya, T.K. Yoo, Development of a web-based ensemble machine learning application to select the optimal size of posterior chamber phakic intraocular lens, *Trans. Vis. Sci. Tech.* 10 (2021) 5–5, doi:[10.1167/tvst.10.6.5](https://doi.org/10.1167/tvst.10.6.5).
- [18] C. Ye, T. Fu, S. Hao, Y. Zhang, O. Wang, B. Jin, M. Xia, M. Liu, X. Zhou, Q. Wu, Y. Guo, C. Zhu, Y.-M. Li, D.S. Culver, S.T. Alfreds, F. Stearns, K.G. Sylvester, E. Widen, D. McElhinney, X. Ling, Prediction of incident hypertension within

- the next year: prospective study using statewide electronic health records and machine learning, *J. Med. Internet Res.* 20 (2018) e22, doi: [10.2196/jmir.9268](https://doi.org/10.2196/jmir.9268).
- [19] N. Tomašev, N. Harris, S. Baur, A. Mottram, X. Glorot, J.W. Rae, M. Zielinski, H. Askham, A. Sarava, V. Maglulo, C. Meyer, S. Ravuri, I. Protsyuk, A. Connell, C.O. Hughes, A. Karthikesalingam, J. Cornebise, H. Montgomery, G. Rees, C. Laing, C.R. Baker, T.F. Osborne, R. Reeves, D. Hassabis, D. King, M. Suleyman, T. Back, C. Nielson, M.G. Seneviratne, J.R. Ledsam, S. Mohamed, Use of deep learning to develop continuous-risk models for adverse event prediction from electronic health records, *Nat. Protoc.* 16 (2021) 2765–2787, doi: [10.1038/s41596-021-00513-5](https://doi.org/10.1038/s41596-021-00513-5).
- [20] B.E. Malyugin, A.A. Shpak, D.F. Pokrovskiy, Accommodative changes in anterior chamber depth in patients with high myopia, *J. Cataract Refractive Surg.* 38 (2012) 1403–1407, doi: [10.1016/j.jcrs.2012.04.030](https://doi.org/10.1016/j.jcrs.2012.04.030).
- [21] S.M. Lundberg, B. Nair, M.S. Vavilala, M. Horibe, M.J. Eisses, T. Adams, D.E. Liston, D.K.-W. Low, S.-F. Newman, J. Kim, S.-I. Lee, Explainable machine-learning predictions for the prevention of hypoxaemia during surgery, *Nat. Biomed. Engineering* 2 (2018) 749, doi: [10.1038/s41551-018-0304-0](https://doi.org/10.1038/s41551-018-0304-0).
- [22] T.H. Rim, C.J. Lee, Y.-C. Tham, N. Cheung, M. Yu, C. Lee, Y. Kim, D.S.W. Ting, C.C.Y. Chong, Y.S. Choi, T.K. Yoo, I.H. Ryu, S.J. Baik, Y.A. Kim, S.K. Kim, S.-H. Lee, B.K. Lee, S.-M. Kang, E.Y.M. Wong, H.C. Kim, S.S. Kim, S. Park, C.-Y. Cheng, T.Y. Wong, Deep-learning-based cardiovascular risk stratification using coronary artery calcium scores predicted from retinal photographs, *Lancet Digital Heal.* 3 (2021) e306–e316, doi: [10.1016/S2589-7500\(21\)00043-1](https://doi.org/10.1016/S2589-7500(21)00043-1).
- [23] T.K. Yoo, J.Y. Choi, H.K. Kim, Feasibility study to improve deep learning in OCT diagnosis of rare retinal diseases with few-shot classification, *Med. Biol. Eng. Comput.* 59 (2021) 401–415, doi: [10.1007/s11517-021-02321-1](https://doi.org/10.1007/s11517-021-02321-1).
- [24] P. Khojasteh, L.A. Passos Júnior, T. Carvalho, E. Rezende, B. Aliahmad, J.P. Papa, D.K. Kumar, Exudate detection in fundus images using deeply-learnable features, *Comput. Biol. Med.* 104 (2019) 62–69, doi: [10.1016/j.combiom.2018.10.031](https://doi.org/10.1016/j.combiom.2018.10.031).
- [25] T. He, J. Guo, N. Chen, X. Xu, Z. Wang, K. Fu, L. Liu, Z. Yi, MediMLP: using grad-cam to extract crucial variables for lung cancer postoperative complication prediction, *IEEE J. Biomed. Heal. Inform.* 24 (2020) 1762–1771, doi: [10.1109/JBHI.2019.2949601](https://doi.org/10.1109/JBHI.2019.2949601).
- [26] A. Saporta, X. Gui, A. Agrawal, A. Pareek, S.Q. Truong, C.D. Nguyen, V.-D. Ngo, J. Seekins, F.G. Blankenberg, A.Y. Ng, M.P. Lungren, P. Rajpurkar, Deep learning saliency maps do not accurately highlight diagnostically relevant regions for medical image interpretation, *MedRxiv* (2021) 2021.02.28.21252634, doi: [10.1101/2021.02.28.21252634](https://doi.org/10.1101/2021.02.28.21252634).
- [27] J.-Y. Zhu, T. Park, P. Isola, A.A. Efros, Unpaired image-to-image translation using cycle-consistent adversarial networks, in: *Proceedings of the IEEE International Conference on Computer Vision*, 2017, pp. 2223–2232.
- [28] S.-M. Shih, P.-J. Tien, Z. Karnin, GANMEX: one-vs-one attributions using GAN-based model explainability, in: *International Conference on Machine Learning*, PMLR, 2021, pp. 9592–9602. <http://proceedings.mlr.press/v139/shih21a.html>.
- [29] J. Harms, Y. Lei, T. Wang, R. Zhang, J. Zhou, X. Tang, W.J. Curran, T. Liu, X. Yang, Paired cycle-GAN-based image correction for quantitative cone-beam computed tomography, *Med. Phys.* 46 (2019) 3998–4009, doi: [10.1002/mp.13656](https://doi.org/10.1002/mp.13656).
- [30] V. Sandfort, K. Yan, P.J. Pickhardt, R.M. Summers, Data augmentation using generative adversarial networks (CycleGAN) to improve generalizability in CT segmentation tasks, *Sci. Rep.* 9 (2019) 16884, doi: [10.1038/s41598-019-52737-x](https://doi.org/10.1038/s41598-019-52737-x).
- [31] K. Bahadarkhan, A.A. Khaliq, M. Shahid, A morphological hessian based approach for retinal blood vessels segmentation and denoising using region based otsu thresholding, *PLoS One* 11 (2016) e0158996, doi: [10.1371/journal.pone.0158996](https://doi.org/10.1371/journal.pone.0158996).
- [32] F. Arcadu, F. Benmansour, A. Maunz, J. Willis, Z. Haskova, M. Prunotto, Deep learning algorithm predicts diabetic retinopathy progression in individual patients, *Npj Digit. Med.* 2 (2019) 1–9, doi: [10.1038/s41746-019-0172-3](https://doi.org/10.1038/s41746-019-0172-3).
- [33] C. Pradhan, S. Khadka, P. Joshi, Angle closure glaucoma in retinitis pigmentosa, Case Report, *Ophthalmol. Med.* 2020 (2020) e6023586, doi: [10.1155/2020/6023586](https://doi.org/10.1155/2020/6023586).
- [34] E. Areiter, M. Neale, S.M. Johnson, Spectrum of angle closure, uveal effusion syndrome, and nanophthalmos, *J. Curr. Glaucoma. Pract.* 10 (2016) 113–117, doi: [10.5005/jp-journals-10008-1211](https://doi.org/10.5005/jp-journals-10008-1211).
- [35] M.M. Ahsan, K.D. Gupta, M.M. Islam, S. Sen, M.L. Rahman, M. Shakhwat Hossein, COVID-19 symptoms detection based on nasnetmobile with explainable AI using various imaging modalities, *Machine Learning. Knowledge Extract.* 2 (2020) 490–504, doi: [10.3390/make2040027](https://doi.org/10.3390/make2040027).
- [36] A. You, J.K. Kim, I.H. Ryu, T.K. Yoo, Application of generative adversarial networks (GAN) for ophthalmology image domains: a survey, *Eye Vision* 9 (2022) 6, doi: [10.1186/s40662-022-00277-3](https://doi.org/10.1186/s40662-022-00277-3).
- [37] M. Frid-Adar, I. Diamant, E. Klang, M. Amitai, J. Goldberger, H. Greenspan, GAN-based synthetic medical image augmentation for increased CNN performance in liver lesion classification, *Neurocomputing* 321 (2018) 321–331, doi: [10.1016/j.neucom.2018.09.013](https://doi.org/10.1016/j.neucom.2018.09.013).
- [38] I.S.A. Abdelhalim, M.F. Mohamed, Y.B. Mahdy, Data augmentation for skin lesion using self-attention based progressive generative adversarial network, expert systems with applications. 165 (2021) 113922. doi: [10.1016/j.eswa.2020.113922](https://doi.org/10.1016/j.eswa.2020.113922).
- [39] H. Emami, M.M. Aliabadi, M. Dong, R.B. Chinnam, SPA-GAN: spatial attention GAN for image-to-image translation, *IEEE Trans. Multimedia* 23 (2021) 391–401, doi: [10.1109/TMM.2020.2975961](https://doi.org/10.1109/TMM.2020.2975961).
- [40] T.K. Yoo, B.Y. Kim, H.K. Jeong, H.K. Kim, D. Yang, I.H. Ryu, Simple code implementation for deep learning-based segmentation to evaluate central serous chorioretinopathy in fundus photography, *Translat. Vision Sci. Technol.* 11 (2022) 22, doi: [10.1167/tvst.11.2.22](https://doi.org/10.1167/tvst.11.2.22).
- [41] S. Pachade, P. Porwal, D. Thulkar, M. Kokare, G. Deshmukh, V. Sahasrabuddhe, L. Giancardo, G. Quellec, F. Mériaudeau, Retinal fundus multi-disease image dataset (RFMiD): a dataset for multi-disease detection research, *Data* 6 (2021) 14, doi: [10.3390/data6020014](https://doi.org/10.3390/data6020014).
- [42] L. Xu, W.F. Cao, Y.X. Wang, C.X. Chen, J.B. Jonas, Anterior chamber depth and chamber angle and their associations with ocular and general parameters: the Beijing eye study, *Am. J. Ophthalmol.* 145 (2008) 929–936 e1, doi: [10.1016/j.ajo.2008.01.004](https://doi.org/10.1016/j.ajo.2008.01.004).
- [43] A. Imran, J. Li, Y. Pei, F. Akhtar, J.-J. Yang, Y. Dang, Automated identification of cataract severity using retinal fundus images, *Comput. Methods Biomed. Engin.* 8 (2020) 691–698, doi: [10.1080/21681163.2020.1806733](https://doi.org/10.1080/21681163.2020.1806733).
- [44] E. Korot, N. Pontikos, X. Liu, S.K. Wagner, L. Faes, J. Huemer, K. Balaskas, A.K. Denniston, A. Khawaja, P.A. Keane, Predicting sex from retinal fundus photographs using automated deep learning, *Sci. Rep.* 11 (2021) 10286, doi: [10.1038/s41598-021-89743-x](https://doi.org/10.1038/s41598-021-89743-x).
- [45] J. Chang, J. Lee, A. Ha, Y.S. Han, E. Bak, S. Choi, J.M. Yun, U. Kang, I.H. Shin, J.Y. Shin, T. Ko, Y.S. Bae, B.-L. Oh, K.H. Park, S.M. Park, Explaining the Rationale of Deep Learning Glaucoma Decisions with Adversarial Examples, *Ophthalmology* (2020), doi: [10.1016/j.ophtha.2020.06.036](https://doi.org/10.1016/j.ophtha.2020.06.036).
- [46] T.K. Yoo, J.Y. Choi, Outcomes of adversarial attacks on deep learning models for ophthalmology imaging domains, *JAMA Ophthalmol.* 138 (2020) 1213–1215, doi: [10.1001/jamaophthalmol.2020.3442](https://doi.org/10.1001/jamaophthalmol.2020.3442).
- [47] E. Tjoa, C. Guan, A survey on explainable artificial intelligence (XAI): toward medical XAI, *IEEE Transac. Neural Networks Learn. Syst.* 32 (2021) 4793–4813, doi: [10.1109/TNNLS.2020.3027314](https://doi.org/10.1109/TNNLS.2020.3027314).
- [48] W. Xiao, X. Huang, J.H. Wang, D.R. Lin, Y. Zhu, C. Chen, Y.H. Yang, J. Xiao, L.Q. Zhao, J.-P.O. Li, C.Y.-L. Cheung, Y. Mise, Z.Y. Guo, Y.F. Du, B.B. Chen, J.X. Hu, K. Zhang, X.S. Lin, W. Wen, Y.Z. Liu, W.R. Chen, Y.S. Zhong, H.T. Lin, Screening and identifying hepatobiliary diseases through deep learning using ocular images: a prospective, multicentre study, *Lancet Digit Health* 3 (2021) e88–e97, doi: [10.1016/S2589-7500\(20\)30288-0](https://doi.org/10.1016/S2589-7500(20)30288-0).
- [49] T.K. Yoo, J.Y. Choi, H.K. Kim, I.H. Ryu, J.K. Kim, Adopting low-shot deep learning for the detection of conjunctival melanoma using ocular surface images, *Comput. Methods Programs Biomed.* 205 (2021) 106086, doi: [10.1016/j.cmpb.2021.106086](https://doi.org/10.1016/j.cmpb.2021.106086).
- [50] A. Bissoto, E. Valle, S. Avila, GAN-based data augmentation and anonymization for skin-lesion analysis: a critical review, in: *2021 IEEE/CVF Conference on Computer Vision and Pattern Recognition Workshops (CVPRW)*, 2021, pp. 1847–1856, doi: [10.1109/CVPRW5098.2021.00204](https://doi.org/10.1109/CVPRW5098.2021.00204).
- [51] H. Qin, R. Gong, X. Liu, X. Bai, J. Song, N. Sebe, Binary neural networks: a survey, *Pattern Recognit.* 105 (2020) 107281, doi: [10.1016/j.patcog.2020.107281](https://doi.org/10.1016/j.patcog.2020.107281).
- [52] A. Krizhevsky, I. Sutskever, G.E. Hinton, Imagenet classification with deep convolutional neural networks, in: *advances in Neural Information Processing Systems*, 2012, pp. 1097–1105.
- [53] H. Qin, R. Gong, X. Liu, M. Shen, Z. Wei, F. Yu, J. Song, Forward and backward information retention for accurate binary neural networks, in: *2020 IEEE/CVF Conference on Computer Vision and Pattern Recognition (CVPR)*, 2020, pp. 2247–2256, doi: [10.1109/CVPR42600.2020.00232](https://doi.org/10.1109/CVPR42600.2020.00232).
- [54] J. Li, X. Liu, M. Zhang, D. Wang, Spatio-temporal deformable 3D ConvNets with attention for action recognition, *Pattern Recognit.* 98 (2020) 107037, doi: [10.1016/j.patcog.2019.107037](https://doi.org/10.1016/j.patcog.2019.107037).
- [55] J. Phu, J. Tong, B. Zangerl, J.L. Le, M. Kalloniatis, Cluster analysis reveals patterns of age-related change in anterior chamber depth for gender and ethnicity: clinical implications, *Ophthalmic Physiol. Optics* 40 (2020) 632–649, doi: [10.1111/opo.12714](https://doi.org/10.1111/opo.12714).
- [56] V. Sarao, D. Veritti, E. Borrelli, S.V.R. Sadda, E. Poletti, P. Lanzetta, A comparison between a white LED confocal imaging system and a conventional flash fundus camera using chromaticity analysis, *BMC Ophthalmol.* 19 (2019) 231, doi: [10.1186/s12886-019-1241-8](https://doi.org/10.1186/s12886-019-1241-8).
- [57] S. VK, X.J.J. Hong, M. Vm, B. M, A. Tin, Progress in anterior chamber angle imaging for glaucoma risk prediction – a review on clinical equipment, practice and research, *Med. Eng. Phys.* 38 (2016) 1383–1391, doi: [10.1016/j.medengphy.2016.09.014](https://doi.org/10.1016/j.medengphy.2016.09.014).
- [58] B.Y. Xu, M. Chiang, S. Chaudhary, S. Kulkarni, A.A. Pardeshi, R. Varma, Deep learning classifiers for automated detection of gonioscopic angle closure based on anterior segment OCT images, *Am. J. Ophthalmol.* 208 (2019) 273–280, doi: [10.1016/j.ajo.2019.08.004](https://doi.org/10.1016/j.ajo.2019.08.004).
- [59] H. Fu, Y. Xu, S. Lin, D.W.K. Wong, M. Baskaran, M. Mahesh, T. Aung, J. Liu, Angle-closure detection in anterior segment OCT based on multilevel deep network, *IEEE Transac. Cybernetics* 50 (2020) 3358–3366, doi: [10.1109/TCYB.2019.2897162](https://doi.org/10.1109/TCYB.2019.2897162).
- [60] W. Wang, L. Wang, X. Wang, S. Zhou, S. Lin, J. Yang, A deep learning system for automatic assessment of anterior chamber angle in ultrasound biomicroscopy images, *Translat. Vision Sci. Technol.* 10 (2021) 21, doi: [10.1167/tvst.10.11.21](https://doi.org/10.1167/tvst.10.11.21).
- [61] Z. Qian, X. Xie, J. Yang, H. Ye, Z. Wang, J. Chen, H. Liu, J. Liang, L. Jiang, C. Zheng, X. Chen, Detection of shallow anterior chamber depth from two-dimensional anterior segment photographs using deep learning, *BMC Ophthalmol.* 21 (2021) 1–9, doi: [10.1186/s12886-021-02104-0](https://doi.org/10.1186/s12886-021-02104-0).
- [62] M. Toğçaçar, N. Muçoğlu, B. Ergen, B.S.B. Yarman, A.M. Halefoğlu, Detection of COVID-19 findings by the local interpretable model-agnostic explanations method of types-based activations extracted from CNNs, *Biomed. Signal Process. Control* 71 (2022) 103128, doi: [10.1016/j.bspc.2021.103128](https://doi.org/10.1016/j.bspc.2021.103128).